Frontiers in Bioscience Landmark

Front. Biosci. (Landmark Ed) **2026**; 31(9): 53668
https://doi.org/10.31083/FBL53668

Original Research

Integrated Transcriptomic and Functional Analyses Identify SERPINE1 as a Ferroptosis-Associated Mediator of Glioblastoma Radioresistance

Yuhang Wang[1], Yanting Li[1], Meng Dong[2], Chao Zeng[1], Zhuanmei Jin[1], Qiuning Zhang[2,*], Wenzhen Yuan[1,*]

[1]The First School of Clinical Medicine, Lanzhou University, 730000 Lanzhou, Gansu, China
[2]Institute of Modern Physics, Chinese Academy of Sciences, 730000 Lanzhou, Gansu, China
*Correspondence: zhangqn@impcas.ac.cn (Qiuning Zhang); yuanwzh@lzu.edu.cn (Wenzhen Yuan)
Academic Editors: Amelia Casamassimi and Sung Eun Kim
Submitted: 8 May 2026 Revised: 30 June 2026 Accepted: 8 July 2026 Published: 14 September 2026

Abstract

Background: Radiotherapy failure remains a major challenge in glioblastoma (GBM), yet the stress-adaptive programs that enable tumor cells to survive irradiation-induced lethal injury remain incompletely defined. This study investigated whether serpin family E member 1 (*SERPINE1*) contributes to GBM radioresistance by modulating ferroptosis-associated lipid peroxidation, a process linked to iron-dependent oxidative injury. **Methods:** Radiotherapy-treated GBM cohorts from TCGA (n = 93; 56 radiosensitive and 37 radioresistant cases), the Chinese Glioma Genome Atlas (CGGA)-325 (n = 100), and CGGA-693 (n = 193), as well as Clinical Proteomic Tumor Analysis Consortium (CPTAC) protein data and the Gene Expression Omnibus (GEO) single-cell RNA sequencing (scRNA-seq) dataset GSE131928, were analyzed using differential gene expression, weighted gene co-expression network analysis (WGCNA), machine-learning feature selection, FerrDb annotation, survival analysis, pathway enrichment, scRNA-seq, and tumor microenvironment (TME) signature profiling. Radiosensitive disease was defined as a complete or partial response after radiotherapy, whereas radioresistant disease was defined as stable or progressive disease. Statistical analyses included Wilcoxon rank-sum tests, Spearman correlations, log-rank tests, multivariable Cox regression for overall survival (OS), and time-dependent receiver operating characteristic (ROC) analysis. Functional validation was performed in two GBM cell lines (U87 and U251) using SERPINE1 knockdown or overexpression, X-ray irradiation, ferrostatin-1 (Fer-1), and RAS-selective lethal 3 (RSL3). **Results:** Integrative screening identified *SERPINE1* as a ferroptosis-associated mediator of radioresistance and poor survival. *SERPINE1* expression was elevated in primary GBM tumors (n = 199) compared with normal tissues (n = 18). *SERPINE1*-high tumors showed enrichment of ferroptosis driver, suppressor, and marker gene signatures, consistent with a ferroptosis-stressed but ferroptosis-defensive state. Single-cell analysis localized *SERPINE1* mainly to mesenchymal-like malignant cells, where high expression co-occurred with hypoxia, extracellular matrix remodeling, radioresistance, and ferroptosis-defense programs. In U87 cells, *SERPINE1* knockdown enhanced radiosensitivity and increased irradiation-induced lipid reactive oxygen species (ROS), malondialdehyde (MDA), and Fe^{2+} accumulation, whereas SERPINE1 overexpression in U251 cells attenuated ferroptosis-associated lipid peroxidation and iron accumulation and improved post-irradiation cell survival. Fer-1 partially rescued the radiosensitizing effect of *SERPINE1* depletion, whereas RSL3 weakened *SERPINE1*-mediated radioprotection. **Conclusions:** *SERPINE1* appears to link mesenchymal adaptation, redox stress regulation, and ferroptosis-associated lipid peroxidation defense in GBM radioresistance. These findings support further evaluation of *SERPINE1*-guided ferroptosis-based radiosensitization strategies. Public datasets were obtained from TCGA, CGGA, CPTAC, and GEO (GSE131928).

Keywords: glioblastoma; plasminogen activator inhibitor 1; radiation tolerance; radiotherapy; ferroptosis; tumor microenvironment; single-cell gene expression analysis

1. Introduction

Glioblastoma (GBM) is the most frequent malignant brain tumor among adults and remains associated with exceptionally poor clinical outcomes, even among aggressive solid tumors [1,2]. Although molecular classification and supportive management have improved, the therapeutic backbone for newly diagnosed disease has changed little: maximal safe resection is followed, when feasible, by radiotherapy with concomitant and adjuvant temozolomide (TMZ) [2,3]. Durable disease control is uncommon. Most tumors recur, and long-term survival remains limited. Accordingly, contemporary reviews increasingly regard treatment resistance, rather than initial treatment response alone, as a central challenge in GBM management [1,2].

Radiotherapy is an essential component of GBM treatment, but its efficacy is limited by cellular heterogeneity and radioresistance. Enhanced DNA damage repair, hypoxia-driven protection, metabolic reprogramming, stem cell-like persistence, and cell-state transitions are all associated with the capacity of GBM cells to tolerate irradiation [4,5]. Mesenchymal differentiation is particularly relevant

Copyright: © 2026 The Author(s). Published by IMR Press.
This is an open access article under the CC BY 4.0 license.

Publisher's Note: IMR Press stays neutral with regard to jurisdictional claims in published maps and institutional affiliations.

because it is closely linked to tumor invasiveness, recurrence, and radiation tolerance [6]. Single-cell studies further show that GBM is not composed of fixed transcriptional subtypes; instead, malignant cells occupy plastic and continuous transcriptional states [7]. Therefore, radiosensitivity is shaped not only by classical intracellular repair mechanisms but also by state-dependent interactions between malignant cells and the surrounding tumor microenvironment.

Ferroptosis is a regulated form of cell death driven by iron-dependent lipid peroxidation [8,9]. In cancer biology, ferroptosis is closely related to redox homeostasis, lipid metabolism, and cellular stress adaptation [9]. Ionizing radiation can induce lipid peroxidation and ferroptosis-related damage, and ferroptosis induction can increase tumor radiosensitivity in multiple contexts [10,11]. The connection between irradiation and lipid peroxidation-mediated cell death therefore provides a rationale for studying ferroptosis as a mechanism of radioresistance and as a potential target for radiosensitization.

In GBM, several ferroptosis-resistance programs have been identified, including *EGFR-ALKBH5* signaling, *NKAP*-mediated *SLC7A11* regulation, control of ferritin autophagy, and mitochondrial stress adaptation [12,13,14,15]. Ferroptosis evasion may also promote radioresistance through regulators such as *IFI16/HMOX1*, *GDF15*, and *POT1-AS1/IGF2BP2/GPX4* [16,17,18]. Meanwhile, the mesenchymal GBM state is closely linked to ferroptosis biology: mesenchymal differentiation promotes radiation resistance, and mesenchymal GBMs can acquire stronger antioxidant defenses, thereby reducing their susceptibility to ferroptosis [6,19]. Ferroptosis resistance may therefore be part of an adaptive phenotype related to mesenchymal plasticity and treatment resistance.

Serpin family E member 1 (*SERPINE1*) has an established but incompletely integrated role in GBM biology. Previous studies have associated *SERPINE1* with GBM invasion and migration, poor prognosis, and a mesenchymal phenotype [20]. Further analysis of the *SERPINE1* interaction network in human GBM suggests that *SERPINE1-linked* proteins contribute to tumor progression, extracellular matrix remodeling, and the regulation of tumor pathways [21]. Hypoxia- and stress-related pathways, including hypoxia-inducible factor 1 alpha (HIF-1α), SMAD family members 2 and 3 (SMAD2/3), and nuclear receptor subfamily 4 group A member 1 (NR4A1)-dependent signaling, can induce or maintain high *SERPINE1* expression [22,23,24]. However, whether *SERPINE1* mediates GBM response to radiotherapy, particularly by regulating radiation-induced ferroptosis-associated lipid peroxidation, remains unclear.

In this study, we integrated radiotherapy-related transcriptomic datasets, machine-learning feature prioritization, FerrDb-guided ferroptosis annotation, and single-cell transcriptomic analysis, followed by functional validation in GBM cell models. *SERPINE1* was identified as a radiotherapy-related candidate gene enriched in mesenchymal, radioresistance, and ferroptosis-defense programs. *SERPINE1* silencing increased radiation-induced lipid peroxidation, ferrous iron accumulation, and radiosensitivity, whereas *SERPINE1* overexpression produced the opposite effects that were partly weakened by ferroptosis induction.

2. Materials and Methods

2.1 Study Design and Data Acquisition

The flowchart of the present study is depicted in Fig. 1. Transcriptomic and clinical data for adult-type glioblastoma, central nervous system (CNS) WHO grade 4 were collected from the TCGA and CGGA databases [25,26]. In the TCGA discovery cohort, 93 radiotherapy-treated patients with documented response data were included in the radiotherapy response analysis, including 56 radiotherapy-sensitive (RS) cases (complete or partial response) and 37 radiotherapy-resistant (RR) cases (stable or progressive disease). The CGGA-325 cohort, which includes detailed radiotherapy records, and the larger CGGA-693 cohort served as independent external validation cohorts. All downstream analyses were performed in these radiotherapy-treated subsets.

2.2 Identification and Functional Enrichment of DEGs

Differential expression analysis between radioresistant (RR) and radiosensitive (RS) groups was performed using an edgeR-voom-limma workflow because this framework handles RNA sequencing (RNA-seq) count dispersion while retaining the flexibility of linear modeling [27,28,29]. After lowly expressed genes were removed, count data were normalized, transformed with voom to account for the mean-variance relationship, and analyzed with empirical Bayes moderation. Transcripts meeting the cutoffs of $|\log2FC| \geq 1$ and adjusted $p < 0.05$ were classified as differentially expressed genes (DEGs). Volcano plots and heatmaps were generated to visualize the distribution and expression trends of these genes. Functional characterization of the DEGs was performed using Gene Ontology (GO) and Kyoto Encyclopedia of Genes and Genomes (KEGG) enrichment analyses with the clusterProfiler package [30].

2.3 Integrated Analysis of WGCNA and Differential Expression

The weighted gene co-expression network analysis (WGCNA) R package was applied to the TCGA-GBM cohort to identify co-expression modules correlated with radiotherapy response [31]. After selection of a soft-thresholding power to approximate scale-free topology, a topological overlap matrix (TOM) was constructed. Genes were grouped into modules by average-linkage clustering and dynamic tree cutting, and closely related modules were merged according to eigengene distances. Pearson correlations between module eigengenes and clinical traits, including radiotherapy status and overall survival, identified

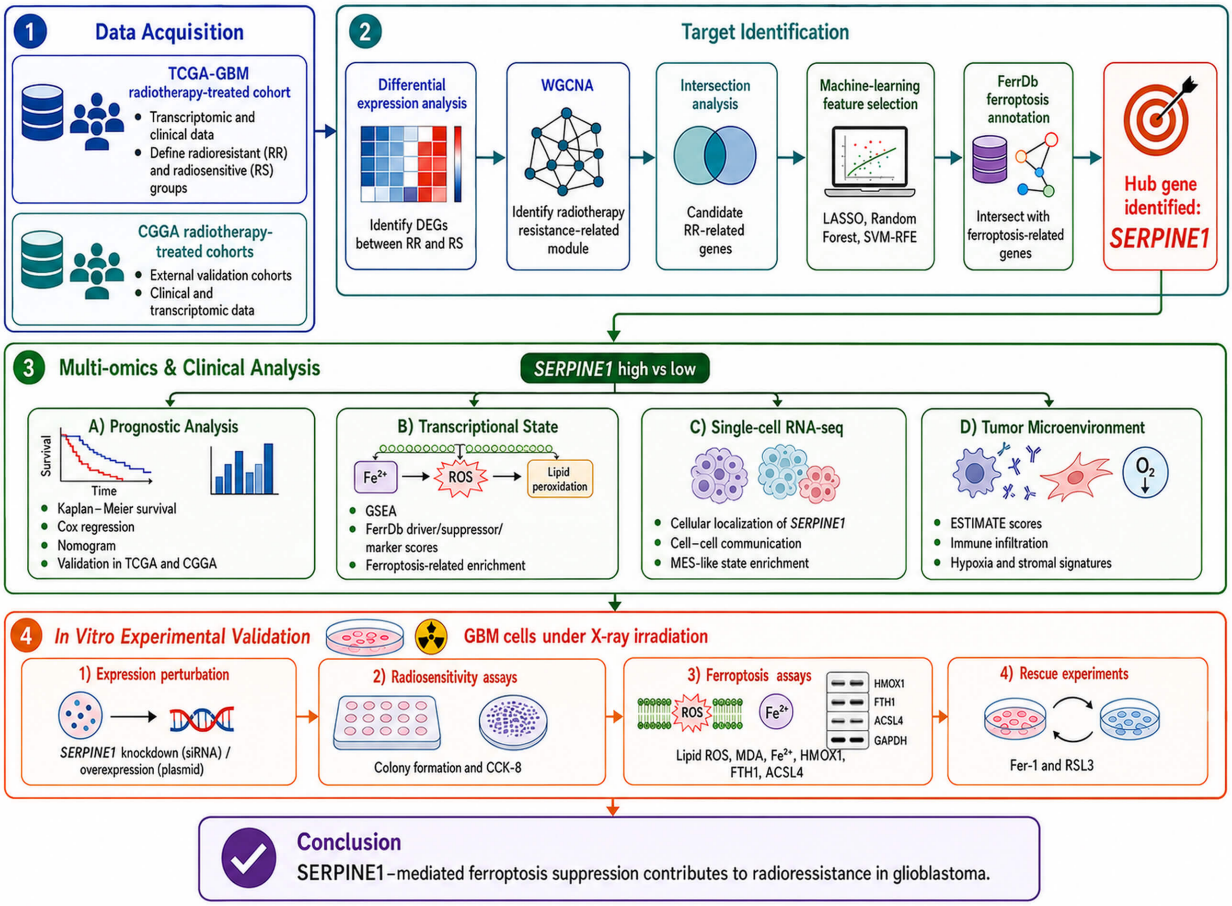

Fig. 1. Flowchart of the comprehensive analysis process in the present study. TCGA, The Cancer Genome Atlas; GBM, glioblastoma; CGGA, Chinese Glioma Genome Atlas; DEGs, differentially expressed genes; WGCNA, weighted gene co-expression network analysis; RR, radiotherapy-resistant; RS, radiotherapy-sensitive; LASSO, least absolute shrinkage and selection operator; SVM-RFE, support vector machine-recursive feature elimination; *SERPINE1*, serpin family E member 1; ROS, reactive oxygen species; MDA, malondialdehyde; CCK-8, Cell Counting Kit-8; *FTH1*, ferritin heavy chain 1; RSL3, RAS-selective lethal 3. Created in BioRender. wang, Y. (2026) https://BioRender.com/7k69rp7.

the primary radioresistance-associated module. Genes from this module were overlapped with the DEGs to obtain candidate radiotherapy resistance-related genes (RRRGs).

2.4 Feature Prioritization by Machine Learning and Ferroptosis Intersection

Three machine-learning frameworks - least absolute shrinkage and selection operator (LASSO) regression with 10-fold cross-validation, Random Forest based on Gini importance, and support vector machine-recursive feature elimination (SVM-RFE) - were used to prioritize the initial radioresistance-related candidates [32,33,34]. The intersection of features selected by the three models was mapped to FerrDb [35] to identify genes annotated as ferroptosis drivers, suppressors, or markers. Genes shared by the machine-learning consensus set and the ferroptosis database were defined as core ferroptosis-associated radioresistance genes for downstream validation.

2.5 Survival and Prognostic Analysis of SERPINE1

Kaplan-Meier analysis and log-rank tests were applied to evaluate the prognostic value of *SERPINE1* for overall survival (OS) in the TCGA-GBM cohort using an optimal expression cutoff derived from maximally selected rank statistics. After external validation in the CGGA-325 and CGGA-693 datasets, a multivariable Cox regression model including *SERPINE1* and age was used to assess whether *SERPINE1* independently predicted OS [36]. Sex was included in the nomogram when available but was not retained in the displayed core Cox forest plot. A prognostic nomogram was developed, and its reliability was assessed using calibration plots. Prognostic accuracy across the three cohorts was evaluated using time-dependent receiver operating characteristic (ROC) analysis [37].

2.6 Gene Set Enrichment and Leading-edge Ferroptosis Program Analysis

Patients were divided into *SERPINE1-high* and *SERPINE1-low* groups using an optimal cutoff value of 8.3518 derived from maximally selected rank statistics in the TCGA cohort, and this cutoff was consistently applied to all validation cohorts. Gene set enrichment analysis (GSEA) was performed using the KEGG ferroptosis pathway (hsa04216) as the reference gene set, and genes were ranked according to differential expression statistics between the two groups [38]. Enrichment was assessed by normalized enrichment score (NES), nominal *p*-value, and false discovery rate (FDR) q-value. The leading-edge subset contained 12 genes: *HMOX1*, *CP*, *STEAP3*, *GCLM*, *SAT1*, *FTL*, *FTH1*, *PCBP1*, *VDAC2*, *ACSL4*, *TFRC*, and *SLC11A2*. Expression values for these genes were log2(x + 1)-transformed and visualized using a row Z-score heatmap. For each sample, a leading-edge ferroptosis score was calculated as the average Z-score of the 12 leading-edge genes. Differences between groups were examined using the Wilcoxon rank-sum test, and the relationship between *SERPINE1* expression and the leading-edge ferroptosis score was determined using Spearman rank correlation analysis.

2.7 Single-cell RNA-seq Analysis

A publicly available single-cell RNA sequencing (scRNA-seq) dataset from IDH-wildtype GBM samples was analyzed. The processed TPM expression matrix was obtained from the Gene Expression Omnibus (GEO), accession number GSE131928. All subsequent scRNA-seq analyses were performed using R software, version 4.5.3 (R Foundation for Statistical Computing, Vienna, Austria) and the Seurat package, version 5.4.0 (Satija Lab, New York, NY, USA). Expression values were log-transformed using the log1p function. After removal of anomalous cells, defined by <500 or >6000 detected genes or >15% mitochondrial reads, highly variable genes were identified using FindVariableFeatures. The dataset was then scaled and processed by principal component analysis (PCA). Based on the first 30 principal components, a nearest-neighbor network was constructed and cells were partitioned into clusters at a resolution of 0.5. Cellular hierarchies were projected and visualized using uniform manifold approximation and projection (UMAP).

2.8 FerrDb-based Analysis of Ferroptosis-related Transcriptional Programs

Curated ferroptosis drivers, suppressors, and markers were obtained from FerrDb. After genes not expressed in the TCGA-GBM matrix were filtered out, the remaining raw counts were normalized using the trimmed mean of M-values (TMM) method and transformed to $\log_2$ counts per million for subsequent analyses. To estimate ferroptotic activity at the individual-sample level, single-sample gene set enrichment analysis (ssGSEA) was applied to compute separate enrichment scores for each of the three functional categories. Patients were divided into *SERPINE1*-high and *SERPINE1*-low groups according to *SERPINE1* expression. Group differences were assessed using the Wilcoxon rank-sum test, and correlations between *SERPINE1* expression and ferroptosis scores were evaluated using Spearman correlation analysis.

2.9 Tumor Microenvironment and Phenotype Signature Analysis

TCGA-GBM raw count data were filtered to remove lowly expressed genes and normalized to $\log_2$ counts per million using edgeR. Tumor microenvironmental composition was evaluated using ESTIMATE-derived StromalScore, ImmuneScore, ESTIMATEScore, and inferred tumor purity. Associations between *SERPINE1* expression and ESTIMATE-derived metrics were assessed using Spearman correlation analysis. To characterize *SERPINE1-associated* tumor ecosystem remodeling, curated TME and malignant phenotype signatures were analyzed by single-sample gene set enrichment analysis (ssGSEA) using the GSVA package. These signatures represented macrophage/microglia, M2 macrophage, cancer-associated fibroblast (CAF)/stromal, endothelial, T cell, cytotoxic T cell, extracellular matrix (ECM) remodeling, EMT/mesenchymal transition, hypoxia, angiogenesis, and GBM transcriptional subtypes. *SERPINE1* was excluded from the GBM mesenchymal signature before ssGSEA scoring to reduce circularity. Group differences were assessed using the Wilcoxon rank-sum test.

2.10 Radioresistance-associated Microenvironmental and Mechanistic Signature Analysis

TCGA-GBM samples were classified into radiosensitive (RS) and radioresistant (RR) groups according to predefined clinical response criteria. Tumor microenvironmental and phenotypic signatures, including M2 macrophage, CAF/stromal, hypoxia, and GBM mesenchymal programs, were compared between RS and RR groups using the Wilcoxon rank-sum test. Continuous associations between *SERPINE1* expression and radioresistance-related programs were evaluated using Spearman correlation analysis. These analyses included the strict GBM mesenchymal signature and mechanism-related signatures representing DNA repair capacity, ROS detoxification, and ferroptosis resistance. The linear regression line is provided for visualization purposes; statistical significance was assessed using Spearman's correlation analysis.

2.11 Cell Lines and Cell Culture

The U251 and U87 human glioblastoma cell lines were provided by the Institute of Modern Physics, Chinese Academy of Sciences (Lanzhou, Gansu, China). Both cell lines were authenticated by short tandem repeat (STR)

profiling and tested negative for mycoplasma before use. Cells were propagated in DMEM (Cat. No. 13072181, Gibco, Grand Island, NY, USA) containing 10% FBS (Cat. No. FND392, ExCell Bio, Suzhou, Jiangsu, China) and 1% penicillin/streptomycin (Cat. No.12610-136, Gibco, Grand Island, NY, USA). Standard incubation conditions (37 °C, 5% CO_2, humidified atmosphere) were applied. Only cells in the logarithmic growth phase were harvested for subsequent assays.

2.12 Small Interfering RNA (siRNA)

SERPINE1 knockdown was performed using si-*SERPINE1*, with a scrambled siRNA as the negative control (si-NC); both were purchased from Shanghai GenePharma Co., Ltd. (Shanghai, China). Cells were transfected using Lipofectamine™ 3000 Transfection Reagent (Cat. No. L3001317, Invitrogen, Carlsbad, CA, USA) according to the manufacturer's protocol. Cells were harvested 48–72 h after transfection for subsequent assays.

2.13 SERPINE1 Overexpression

SERPINE1-overexpression plasmids and matched control vectors (Shanghai GenePharma Co., Ltd., Shanghai, China) were transfected into U251 cells using Lipofectamine 3000 (Invitrogen, USA) according to the manufacturer's protocol. Cells were harvested 48–72 h after transfection. Ectopic *SERPINE1* expression was confirmed by RT-qPCR and Western blotting.

2.14 Quantitative Real-time PCR

After total RNA extraction and reverse transcription, *SERPINE1* mRNA abundance was measured by RT-qPCR using a SYBR Green master mix according to the manufacturer's protocol. Expression values were normalized to GAPDH. The primer sequences were as follows: *SERPINE1* F: 5′-CACAAATCAGACGGCAGCACT-3′, R: 5′-CATCGGGCGTGGTGAACTC-3′; *GAPDH* F: 5′-TGCACCACCAACTGCTTAGC-3′, R: 5′-GGCATGGACTGTGGTCATGAG-3′. Relative transcript abundance was calculated using the $2^{-\Delta\Delta Cq}$ method.

2.15 Western Blotting

Total protein lysates from U87 and U251 cells were prepared in RIPA buffer containing 1% protease inhibitor and quantified using the Pierce™ BCA Protein Assay Kit (Cat. No. 23227, Thermo Fisher Scientific, Waltham, MA, USA). For each sample, 30 µg of protein was separated by 10% SDS-PAGE and transferred to Millipore PVDF membranes. After blocking with 5% non-fat milk/TBST for 1 h at room temperature, membranes were incubated overnight at 4 °C with primary antibodies against SERPINE1 (1:1000, Cat. No. ab66705), FTH1 (1:1000, Cat. No. ab75973), HMOX1 (1:1000, Cat. No. ab52947), ACSL4 (1:1000, Cat. No. ab155282) and GAPDH (1:5000, Cat. No. ab8245; all from Abcam, Cambridge, UK). After washing with TBST, membranes were incubated with IRDye 800CW-labeled goat anti-mouse (1:10,000, Cat. No. ab216772) or anti-rabbit secondary antibodies (1:10,000, Cat. No. ab216773, Abcam, Cambridge, UK). Immunoreactive bands were scanned using an Odyssey CLx infrared imaging system and quantified with Image Studio software (LI-COR Biosciences, Lincoln, NE, USA).

2.16 Cell Irradiation and Reagents

Cells were exposed to 0, 2, 4, or 6 Gy X-rays for radiosensitivity assays using a Precision X-Ray X-RAD 225 generator operated at 225 kV and 13.3 mA, with a 40-cm source-to-target distance, a 0.2-mm Al filter, and a dose rate of 2.0–3.0 Gy/min. For pharmacological interventions, the ferroptosis inhibitor Fer-1 (1 µM, Cat. No. HY-100579) and inducer RSL3 ((1S,3R)-RSL3; 0.5 µM, Cat. No. HY-100218A) were dissolved in DMSO (Cat. No. C0672301190, Nanjing Chemical Reagent Co., Ltd., Nanjing, Jiangsu, China) to prepare 1 mM stock solutions. Before irradiation, cells were treated with 1 µM Fer-1 or 0.5 µM RSL3 for 2 h.

2.17 Colony Formation Assay

U87 and U251 cells were seeded in 60 mm culture dishes at densities adjusted according to radiation dose and then irradiated with 0, 2, 4, or 6 Gy of X-rays. Twelve to fourteen days after irradiation, surviving colonies were fixed with 4% paraformaldehyde (Cat. No. P9729, Solarbio, Beijing, China) and stained with crystal violet (Cat. No. G5122, Solarbio, Beijing, China). Colonies containing at least 50 cells were counted. Plating efficiency (PE) was calculated as the number of colonies divided by the number of cells seeded at 0 Gy irradiation. The surviving fraction (SF) was obtained by dividing the colony formation efficiency at each radiation dose by the corresponding PE value. The experiment was performed in three independent biological replicates.

$$SF = \exp\left[-\left(\alpha D + \beta D^2\right)\right] \quad (1)$$

where D represents radiation dose, and α and β represent the linear and quadratic components of radiation-induced cell death, respectively.

2.18 Cell Counting Kit-8 (CCK-8) Assay

After transfection, U87 and U251 cells (500–3000 cells/well in 96-well plates) were exposed to 0 or 4 Gy X-rays after attachment. Cell viability was measured at 0, 24, 48, and 72 h after irradiation using the CCK-8 assay (10 µL/well, Cat. No. HY-K0301, MedChemExpress, Monmouth Junction, NJ, USA). After adding 10 µL of CCK-8 reagent and incubating for 2 h at 37 °C with 5% CO_2, absorbance at 450 nm was measured using a microplate reader. Data were obtained from three independent biological experiments, each with internal technical replicates.

2.19 Lipid ROS Detection

Cellular lipid reactive oxygen species (lipid ROS) levels were measured using the BODIPY™ 581/591 C11 probe (Cat. No. HY-D2511, MedChemExpress, Monmouth Junction, NJ, USA). After the indicated treatments, including transfection and X-ray irradiation, U87 and U251 cells were washed twice with PBS and incubated with 5 μM BODIPY 581/591 C11 for 30 min at 37 °C in the dark. Cells were then collected, washed, and resuspended in 500 μL PBS for flow cytometry analysis. Fluorescence signals of oxidized C11-BODIPY were detected using the FITC channel, with at least 10,000 events collected for each sample. The level of lipid ROS was first quantified by mean fluorescence intensity (MFI), then normalized to the corresponding control group, and expressed as fold change for subsequent statistical analysis and graphing.

2.20 Malondialdehyde (MDA) Assay

Lipid peroxidation was assessed by measuring intracellular malondialdehyde (MDA). After treatment, cells were collected, washed with PBS, and sonicated on ice. Supernatants were analyzed using a commercial MDA kit (Cat. No. BC0163, Solarbio, Beijing, China) according to the manufacturer's protocol. Absorbance values were normalized to total protein concentration, and MDA levels were expressed as fold changes relative to the untreated control group.

2.21 Measurement of Fe^{2+}

Intracellular Fe^{2+} levels were quantified using a Ferrous Ion Assay Kit (Cat. No. BC9109, Solarbio, Beijing, China) according to the manufacturer's protocol. Fe^{2+} values were normalized to total protein concentration and are presented as relative intracellular Fe^{2+} levels.

2.22 Statistical Analysis

Statistical analyses were conducted using R, version 4.5.3 (R Foundation for Statistical Computing, Vienna, Austria) for bioinformatics and GraphPad Prism, version 9.0.2 (GraphPad Software, Boston, MA, USA) for experimental assays. Quantitative results are presented as mean ± standard deviation (SD) from at least three independent biological replicates. Intergroup differences were assessed using unpaired two-tailed Student's *t*-tests for two normally distributed groups, Wilcoxon rank-sum tests for non-parametric data, or one-/two-way analysis of variance (ANOVA) with appropriate post-hoc tests (Tukey's or Šídák's) for multiple comparisons. Prognostic analyses used Kaplan-Meier survival curves with log-rank tests and multivariable Cox regression, and predictive utility was quantified by time-dependent ROC analysis. Associations between continuous variables were evaluated by Spearman correlation. For GSEA, NES, nominal *p*-values, and FDR q-values were recorded. Significance was established at a two-tailed $p < 0.05$; specific statistical tests are stated in the corresponding figure legends.

3. Results

3.1 Differential Expression and Enrichment Analyses

Differential expression analysis identified 268 DEGs between the RR and RS groups, including 160 upregulated and 108 downregulated genes in the RR group (Fig. 2A). Representative upregulated genes included *BMP5*, *MMP13*, and *COL6A3*, whereas *TPTEP1*, *LINC00689*, and *NOS2* were among the downregulated genes. Unsupervised hierarchical clustering of the top 50 DEGs clearly separated RR from RS samples, indicating distinct transcriptional profiles (Fig. 2B). GO enrichment analysis showed that these DEGs were mainly associated with extracellular matrix remodeling and microenvironment-related biological processes, including extracellular matrix organization, external encapsulating structure organization, ossification, epithelial cell proliferation, and negative regulation of Wnt signaling (Fig. 2C). KEGG pathway analysis further revealed significant enrichment in cytokine-cytokine receptor interaction, protein digestion and absorption, focal adhesion, IL-17 signaling, and ECM-receptor interaction pathways (Fig. 2D).

3.2 Construction of WGCNA Co-expression Network and Identification of Key Modules

WGCNA was applied to expression profiles from radiotherapy-treated patients. Hierarchical clustering revealed no distinct outliers; therefore, all samples were incorporated into the network (Fig. 3A). A soft-thresholding value of beta = 7 was adopted to approximate a scale-free topology (Fig. 3B). After TOM-based clustering and dynamic tree cutting with a module merge cut height of 0.25, 19 valid non-grey modules were generated (Fig. 3C). Module-trait analysis identified the light green module as the primary candidate module because it showed a positive association with radioresistance ($R = 0.26$, $p = 0.01$) and a negative association with patient survival ($R = –0.22$, $p = 0.03$) (Fig. 3D). Intersecting genes in this module with the 268 DEGs yielded six essential RRRGs: *SERPINE1*, *SFRP2*, *MMP13*, *LOX*, *ASPN*, and *CXCL13*.

3.3 Identification of SERPINE1 via Machine Learning and Ferroptosis Database

To further refine the candidate genes, three machine learning algorithms, including LASSO, Random Forest, and SVM-RFE, were applied. Each method identified a subset of informative genes (Fig. 4A–C), and intersection of the three models yielded two common candidates, *SERPINE1* and *LOX* (Fig. 4D). Further comparison with the FerrDb database showed that both genes were ferroptosis-related. Among them, *SERPINE1* was annotated as a ferroptosis suppressor, which is consistent with the radioresistant phenotype examined in this study.

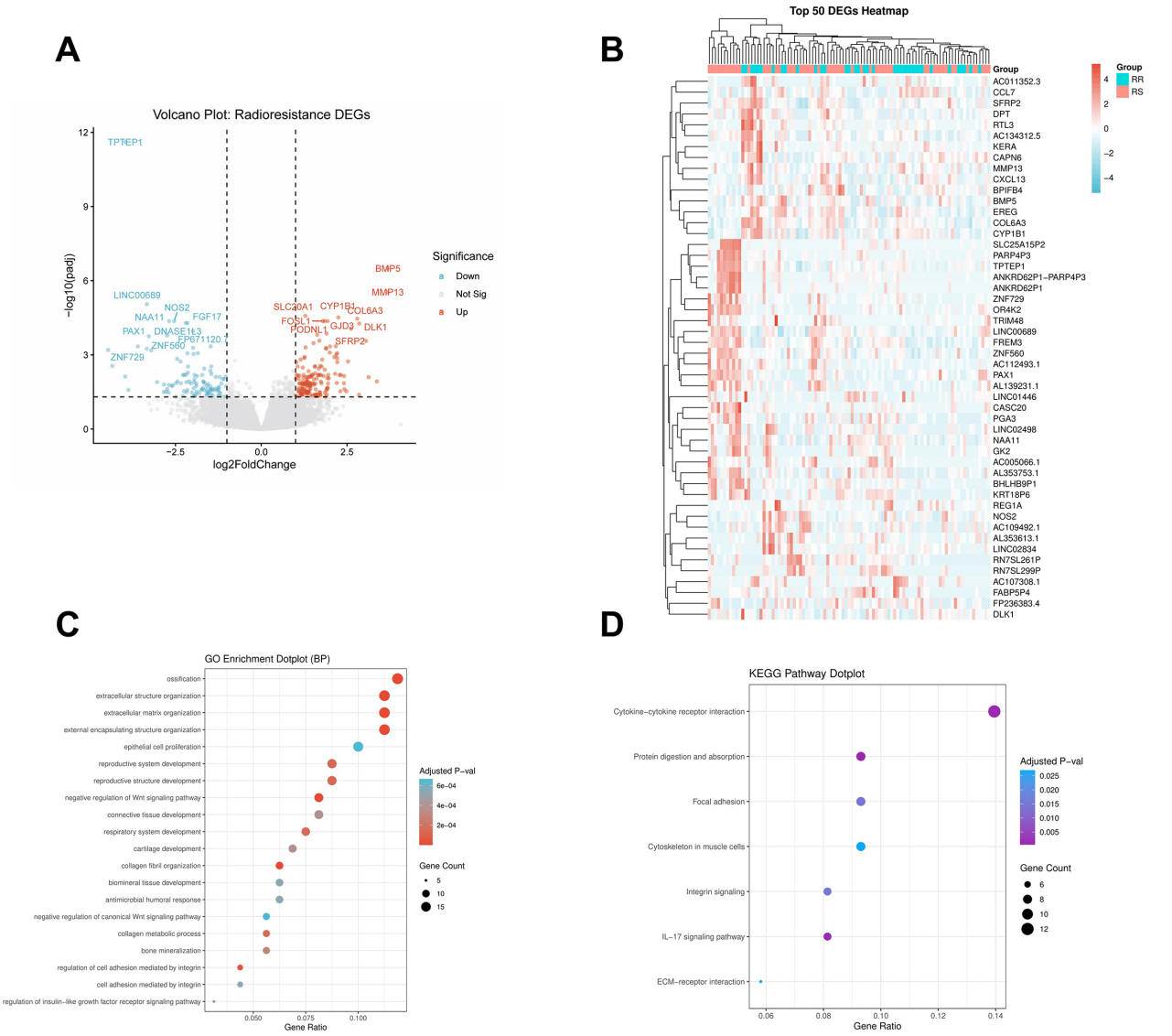

Fig. 2. Differential-expression and enrichment analyses between radiotherapy-resistant and radiotherapy-sensitive GBM samples. (A) Volcano plot showing DEGs between RR and RS groups. (B) Heatmap of the top 50 DEGs. (C) GO enrichment analysis of DEGs. (D) KEGG pathway enrichment analysis, highlighting extracellular matrix, focal adhesion, cytokine signaling, interleukin-17 (IL-17) signaling, and ECM-receptor interaction pathways.

3.4 SERPINE1 is Upregulated in GBM and Predicts Unfavorable Survival

Analysis of CPTAC data demonstrated significantly higher *SERPINE1* levels in primary GBM tumors (n = 199) than in normal tissues (n = 18; $p = 1.53 \times 10^{-10}$), highlighting its association with tumor malignancy (Fig. 5A). High *SERPINE1* expression was associated with shorter survival across three independent cohorts: TCGA-GBM (n = 93; HR = 1.73, $p = 0.024$), CGGA-325 (n = 100; HR = 2.06, $p = 0.009$), and CGGA-693 (n = 193; HR = 2.68, $p = 0.002$) (Fig. 5B–D). Detailed characteristics of the GBM cohorts are summarized in **Supplementary Table 1**. Multivariable adjustment confirmed that *SERPINE1* (HR = 3.38, $p = 0.030$) and age ≥60 years (HR = 2.75, $p = 0.045$) were independent prognostic determinants (Fig. 5E).

A clinical nomogram combining *SERPINE1*, age, and sex was developed using the CGGA-693 cohort and showed adequate 12-month calibration agreement (Fig. 5F,G). Time-dependent ROC analyses revealed moderate and cohort-specific discriminative power. The respective 6-, 12-, and 18-month areas under the curve (AUCs) were 0.602, 0.658, and 0.619 in the TCGA cohort; 0.442, 0.503, and 0.611 in CGGA-325; and 0.616, 0.548, and 0.584 in CGGA-693 (**Supplementary Fig. 1A–C**).

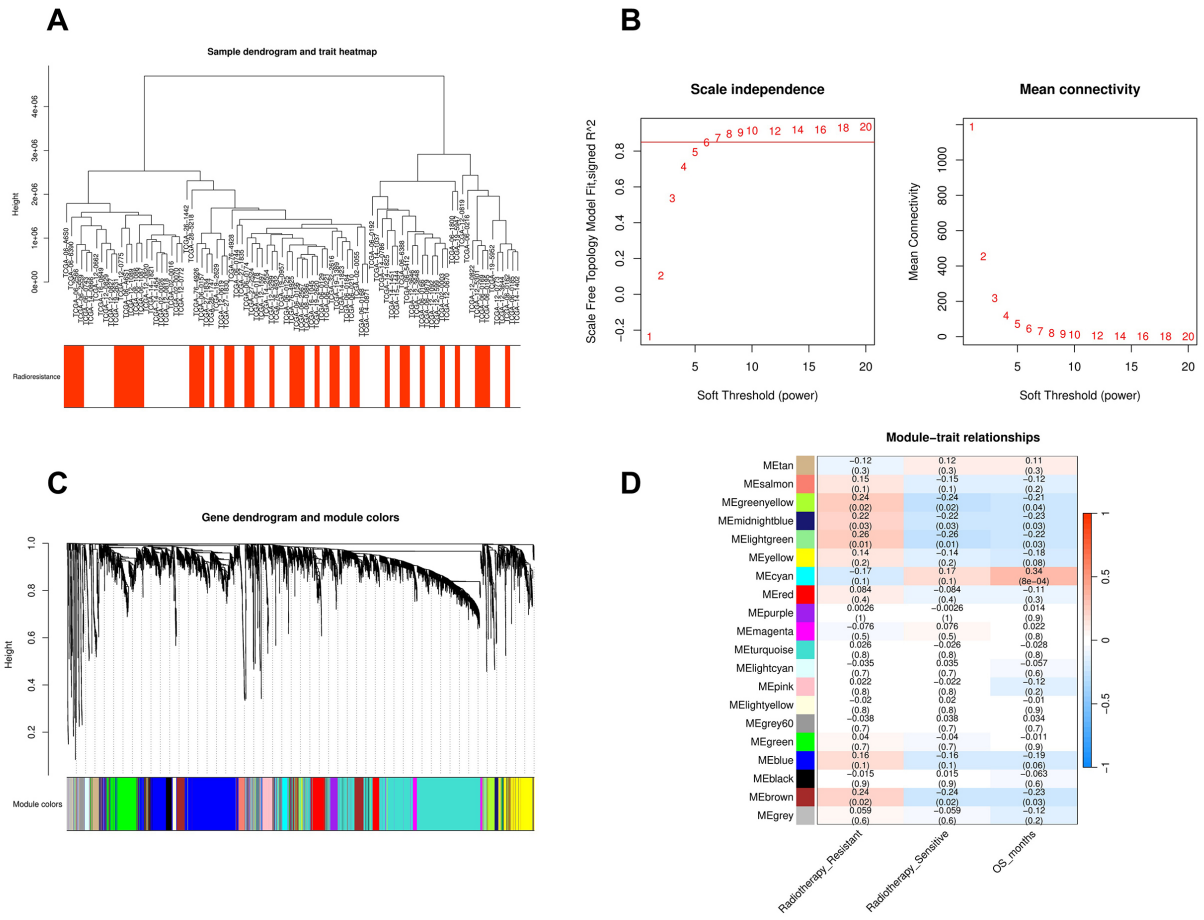

Fig. 3. WGCNA identifies radiotherapy-resistance-associated co-expression modules. (A) Sample clustering of radiotherapy-treated GBM patients. (B) Soft-thresholding power selection based on scale-free topology and mean connectivity. (C) Gene dendrogram and module assignment after dynamic tree cutting and module merging. (D) Module-trait relationship heatmap showing the association of co-expression modules with radiotherapy resistance and overall survival.

3.5 SERPINE1-high GBM Exhibits a Ferroptosis-stressed and Ferroptosis-defensive Transcriptional State

GSEA revealed significant enrichment of the KEGG ferroptosis pathway in the *SERPINE1*-high group relative to the *SERPINE1*-low group (Fig. 6A; NES = 2.08, nominal $p < 0.001$, FDR q < 0.001), indicating an association between elevated *SERPINE1* expression and a ferroptosis-related transcriptional signature. The leading-edge subset comprised 12 genes, which collectively displayed a shift toward higher standardized expression in the *SERPINE1*-high group (Fig. 6B). To summarize this pattern at the sample level, a leading-edge ferroptosis score was calculated as the mean Z-score of the 12 leading-edge genes; this score was significantly higher in the *SERPINE1*-high group (Fig. 6C; $p = 3.3 \times 10^{-9}$) and positively correlated with *SERPINE1* expression (Fig. 6D; Spearman ρ = 0.57, $p = 9.3 \times 10^{-16}$). Consistently, representative ferroptosis-related genes, including *HMOX1*, *FTH1*, and *ACSL4*, were expressed at higher levels in the *SERPINE1*-high group (Fig. 6E; $p = 7.4 \times 10^{-10}$, 8.1×10^{-5}, and 0.0022, respectively).

3.6 SERPINE1-high GBM Exhibits Coordinated Ferroptosis-related Stress and Anti-ferroptotic Defense Programs

Because enrichment of ferroptosis pathway genes does not necessarily indicate ferroptotic cell death, we next examined the directionality of ferroptosis-related transcriptional remodeling using FerrDb-defined functional categories. FerrDb-annotated genes were classified into ferroptosis drivers, suppressors, and markers, and category-specific ssGSEA scores were calculated in the TCGA-GBM cohort. Compared with *SERPINE1*-low tumors, *SERPINE1*-high tumors exhibited significantly higher enrichment scores for ferroptosis drivers, suppressors, and markers (Fig. 7A; Wilcoxon rank-sum test, $p = 1.03 \times 10^{-13}$, $p = 9.30 \times 10^{-10}$, and $p = 1.06 \times 10^{-25}$, respectively). Consistently, *SERPINE1* expression was positively correlated with the ferroptosis-driver score, ferroptosis-suppressor score, and ferroptosis-marker score, with Spearman correlation coefficients of ρ = 0.50, ρ = 0.35, and ρ = 0.57, respectively, all with $p < 0.001$ (Fig. 7B).

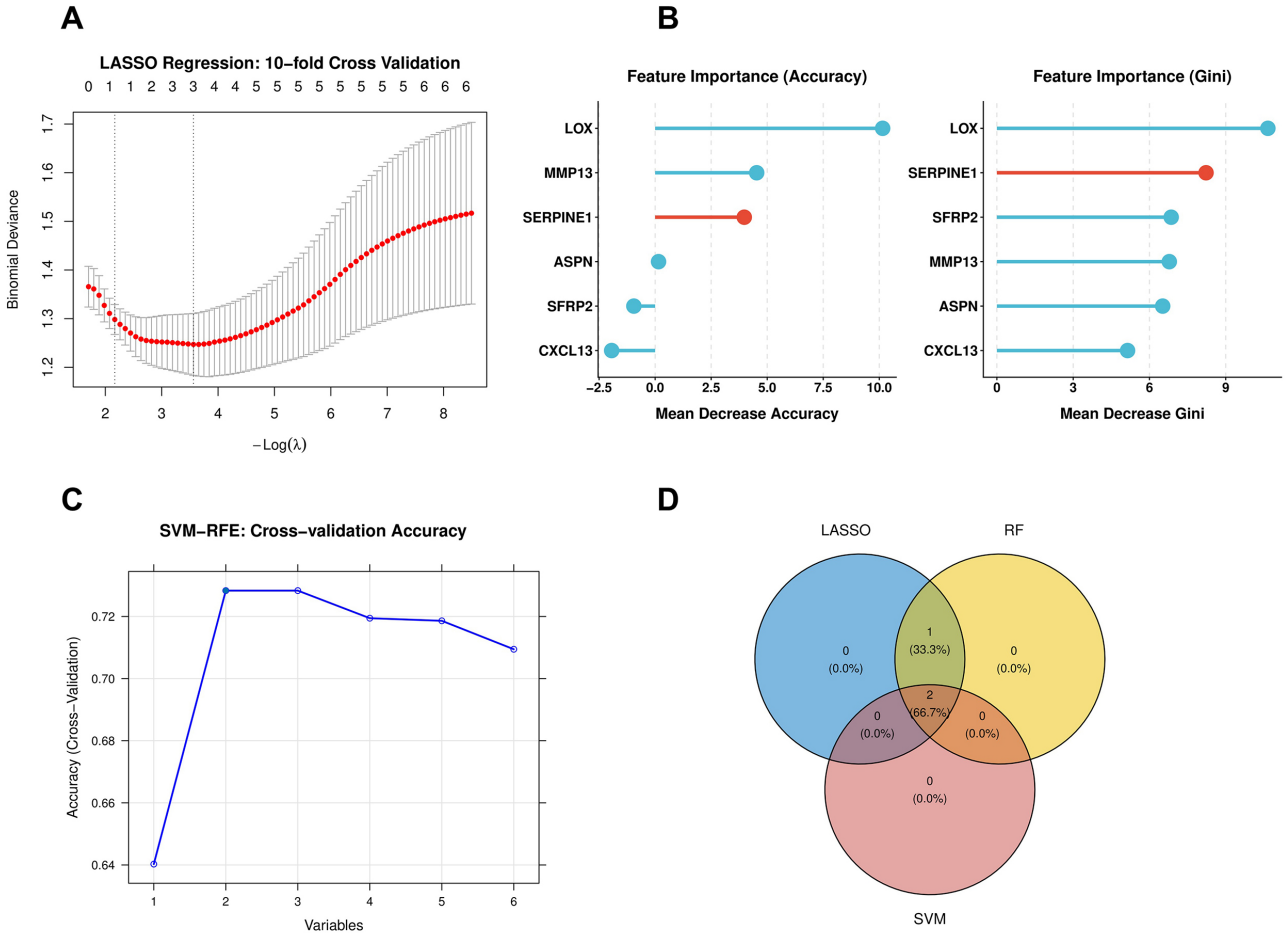

Fig. 4. Machine-learning prioritization of candidate genes. (A) LASSO feature selection. (B) Random Forest feature-importance ranking. (C) SVM-RFE feature selection. (D) Intersection of candidate genes selected by the three algorithms, identifying *SERPINE1* and *LOX* as common candidates.

3.7 Single-cell Analysis Localizes SERPINE1 Expression to MES-like Malignant Cells With Ferroptosis-defense and Radioresistance Programs

Having established a bulk-level association between *SERPINE1* expression and ferroptosis-related remodeling, we next investigated the cellular compartment contributing to this phenotype using a public single-cell RNA-seq dataset of IDH-wildtype GBM. After quality control, clustering, and UMAP dimensionality reduction, cells were annotated into malignant core cells, MES-like malignant cells, myeloid/microglial cells, oligodendrocyte-lineage cells, T cells, and unknown populations based on canonical marker genes (Fig. 8A).

SERPINE1 expression showed marked cellular heterogeneity. UMAP feature plots and dot plots revealed preferential enrichment of *SERPINE1* in MES-like malignant cells, whereas weaker expression was observed in myeloid/microglial cells and relatively low expression was detected in T cells and oligodendrocyte-lineage cells (Fig. 8B,C). These findings suggest that bulk *SERPINE1* expression in GBM may partly reflect a MES-like malignant cell state rather than uniform expression across all cell populations.

We next compared functional module scores between *SERPINE1*-high and SERPINE1-low cells among *SERPINE1*-positive cells. *SERPINE1*-high cells showed significantly higher scores for ferroptosis drivers, ferroptosis suppressors, hypoxia, extracellular matrix remodeling, MES-like state, and radioresistance (Fig. 8D). The concurrent elevation of ferroptosis-driver and ferroptosis-suppressor programs suggests that *SERPINE1*-high cells may represent a ferroptosis-stressed but ferroptosis-defensive state. In addition, the enrichment of hypoxia, ECM, MES-like, and radioresistance programs indicates that *SERPINE1* expression is associated with a stress-adaptive and therapy-resistant malignant cell state.

3.8 SERPINE1-high GBM is Associated With Stromal Remodeling, Immune Infiltration, Hypoxia, and Mesenchymal Transition

Given the enrichment of *SERPINE1* in MES-like malignant cells and its association with hypoxia- and

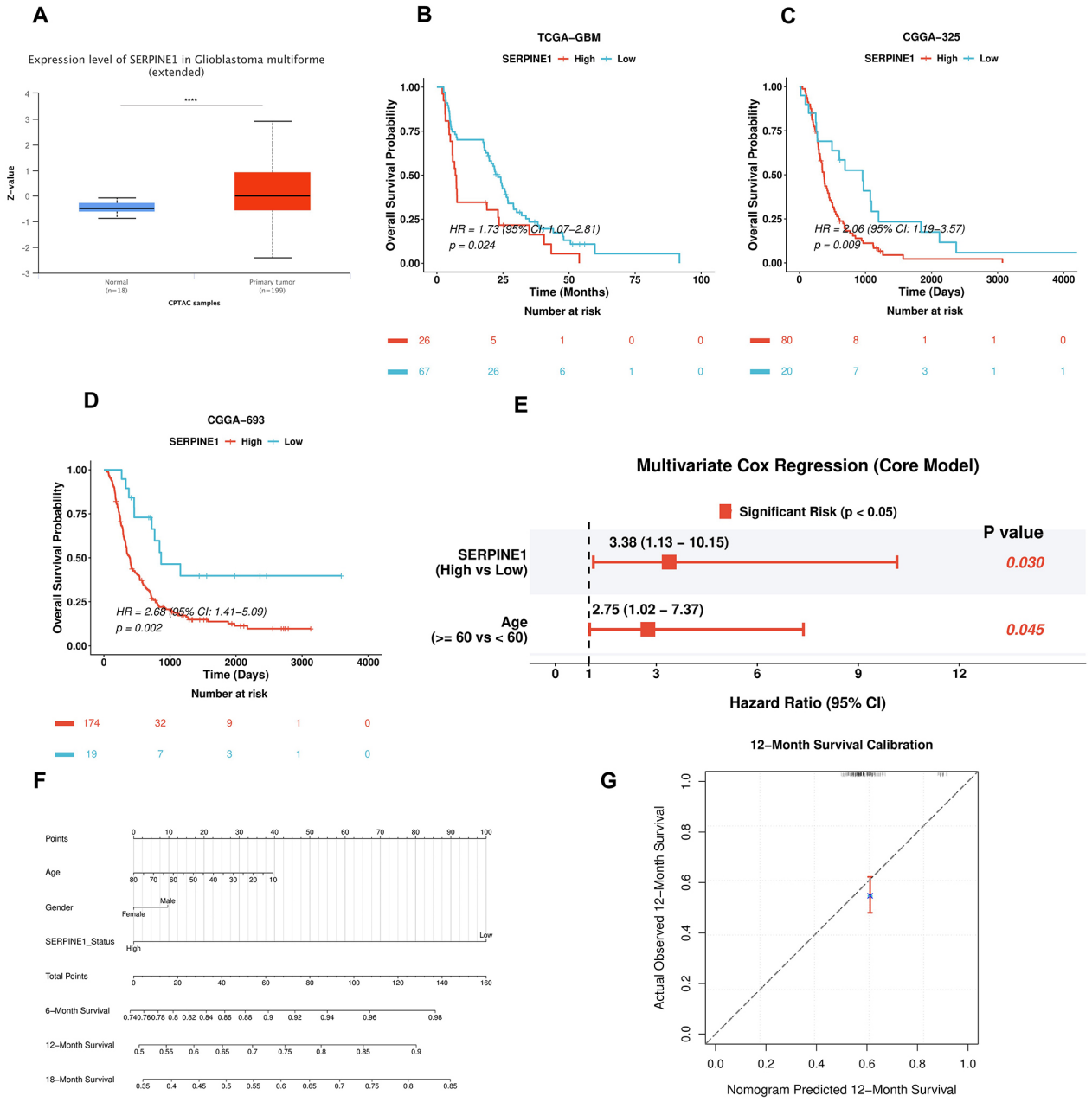

Fig. 5. *SERPINE1* expression and prognostic validation in GBM cohorts. (A) SERPINE1 expression level in CPTAC glioblastoma samples comparing normal brain tissues and primary GBM tumors. SERPINE1 expression was significantly higher in primary GBM tumors than in normal tissues. (B–D) Kaplan-Meier survival curves comparing SERPINE1-high and SERPINE1-low groups in the TCGA-GBM, CGGA-325, and CGGA-693 cohorts; number-at-risk tables are shown below each curve. (E) Multivariable Cox regression analysis including SERPINE1 expression and clinical variables. (F) Nomogram incorporating SERPINE1 status and clinical factors for survival prediction. (G) Calibration curve comparing predicted and observed 12-month survival.

radioresistance-related programs, we next examined whether *SERPINE1*-high tumors also displayed bulk-level tumor microenvironmental remodeling. ESTIMATE analysis showed that *SERPINE1* expression was positively correlated with StromalScore and ImmuneScore, but negatively correlated with inferred tumor purity, with Spearman correlation coefficients of $\rho = 0.45$, $\rho = 0.47$, and $\rho = -0.47$, respectively, all with $p < 0.001$ (Fig. 9A). These results suggest that *SERPINE1*-high GBM is associated with increased stromal and immune components within the tumor ecosystem.

ssGSEA-based signature analysis further showed that SERPINE1-high tumors had significantly elevated macrophage/microglia, M2 macrophage, CAF/stromal, en-

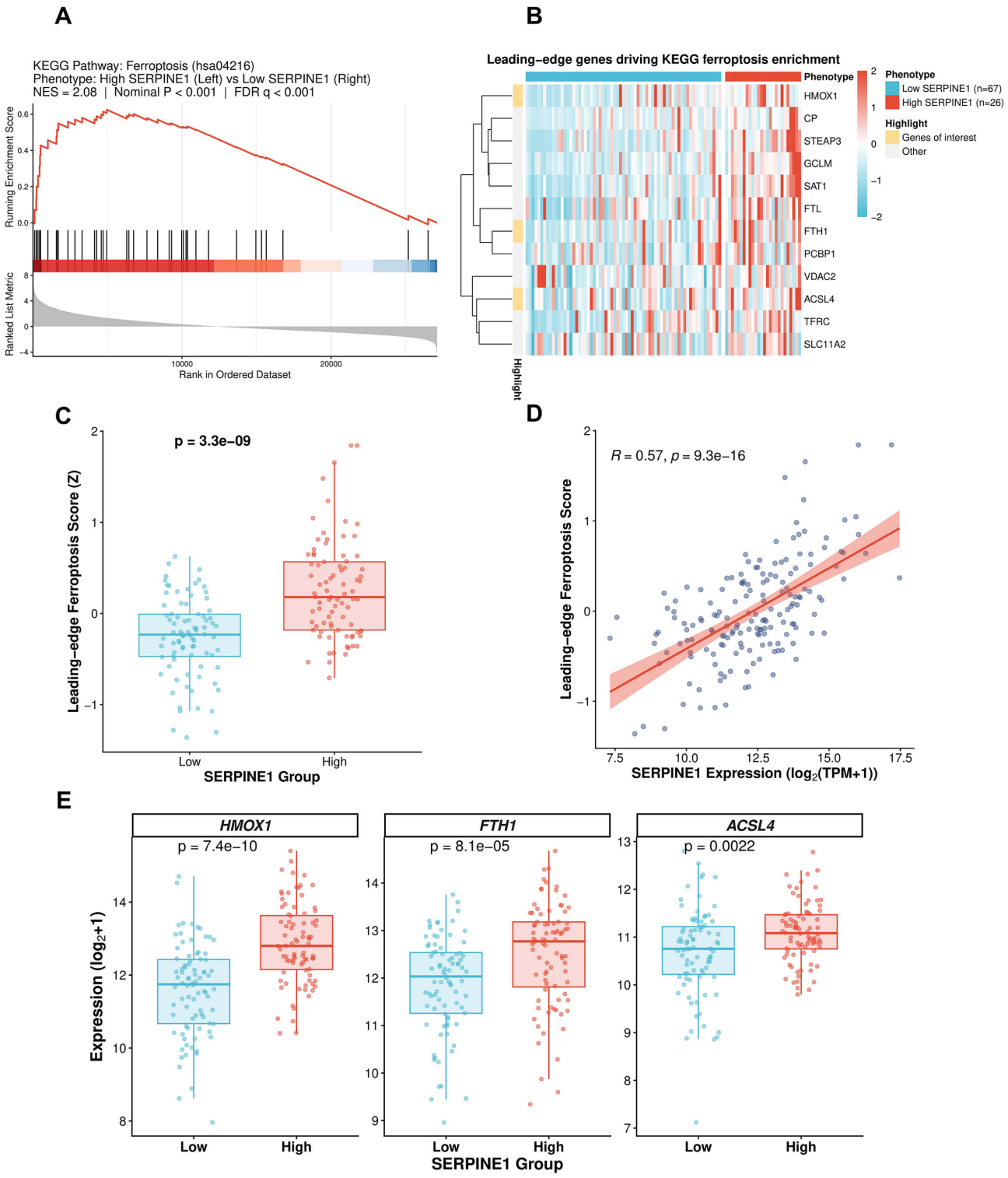

Fig. 6. *SERPINE1*-high GBM is associated with ferroptosis-related leading-edge transcriptional enrichment. (A) GSEA plot of the KEGG ferroptosis pathway in *SERPINE1*-high versus *SERPINE1*-low tumors. (B) Heatmap of 12 leading-edge ferroptosis genes. (C) Leading-edge ferroptosis score comparison between *SERPINE1*-high and *SERPINE1*-low groups. (D) Spearman correlation between *SERPINE1* expression and the leading-edge ferroptosis score. (E) Expression of representative ferroptosis-related genes HMOX1, FTH1, and ACSL4 between *SERPINE1* expression groups.

dothelial, ECM remodeling, EMT/mesenchymal, GBM mesenchymal, and hypoxia scores compared with *SERPINE1*-low tumors (Fig. 9B). T-cell and cytotoxic T-cell signatures were also modestly but significantly increased in

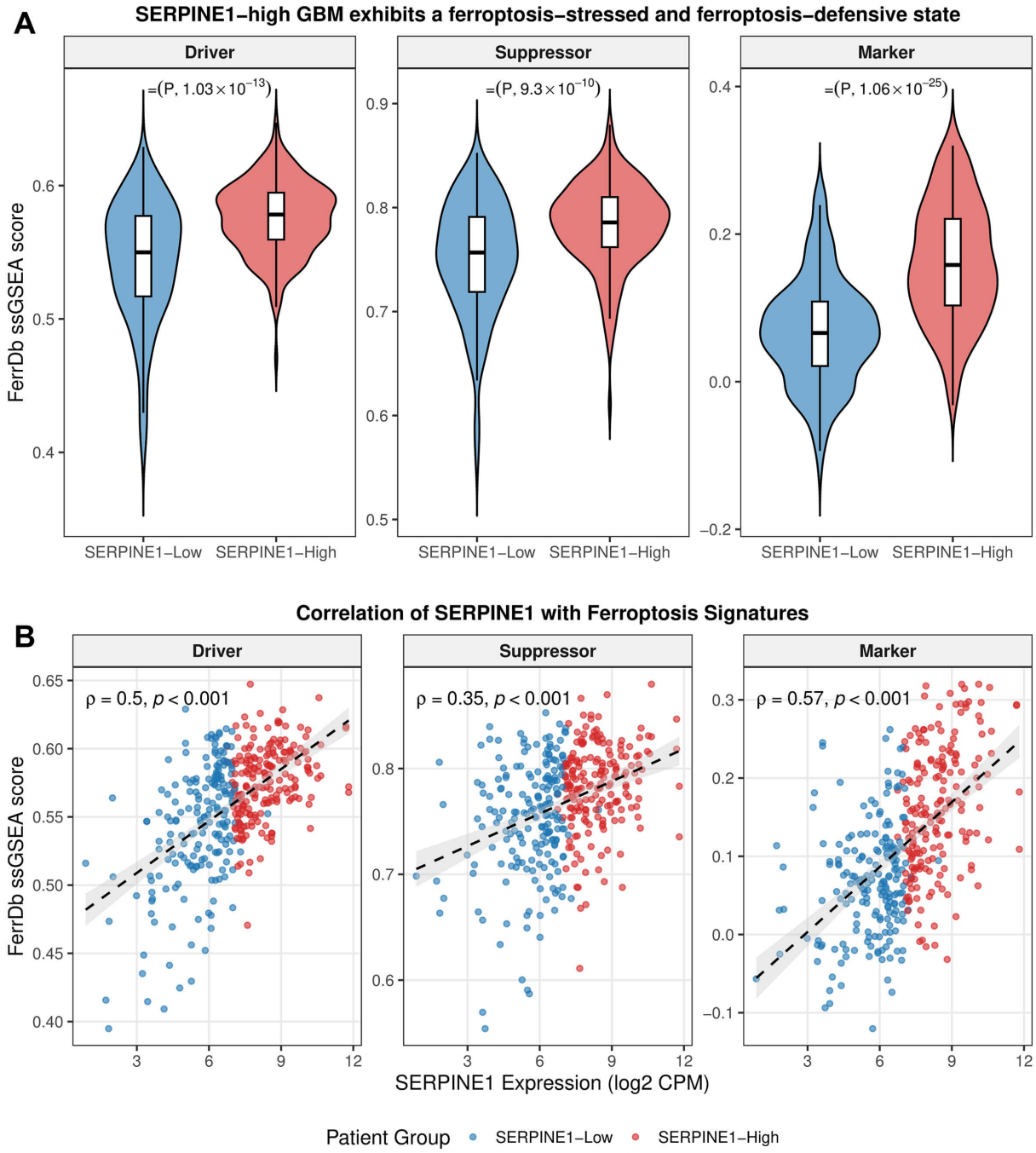

Fig. 7. FerrDb-based analysis distinguishes ferroptosis-related stress from anti-ferroptotic defense in *SERPINE1*-high GBM. (A) FerrDb-annotated ferroptosis genes were classified into driver, suppressor, and marker categories, and category-specific ssGSEA scores were compared between *SERPINE1*-low and *SERPINE1*-high tumors in the TCGA-GBM cohort. *SERPINE1*-high tumors showed significantly higher scores across all three ferroptosis-related categories. (B) Spearman correlation analysis showed positive associations between *SERPINE1* expression and FerrDb-defined driver, suppressor, and marker scores. These results support the presence of a ferroptosis-stressed but ferroptosis-defensive transcriptional state in *SERPINE1*-high GBM. GBM, glioblastoma; ssGSEA, single-sample gene set enrichment analysis.

SERPINE1-high tumors. Together, these findings indicate that *SERPINE1*-high GBM is associated with a broadly remodeled tumor ecosystem characterized by myeloid enrichment, stromal activation, vascular and ECM remodeling, hypoxia, and mesenchymal transition. Correlation analysis confirmed that SERPINE1 expression was positively associated with multiple TME cell-state signatures, stromal and malignant programs, and the GBM mesenchymal sub-

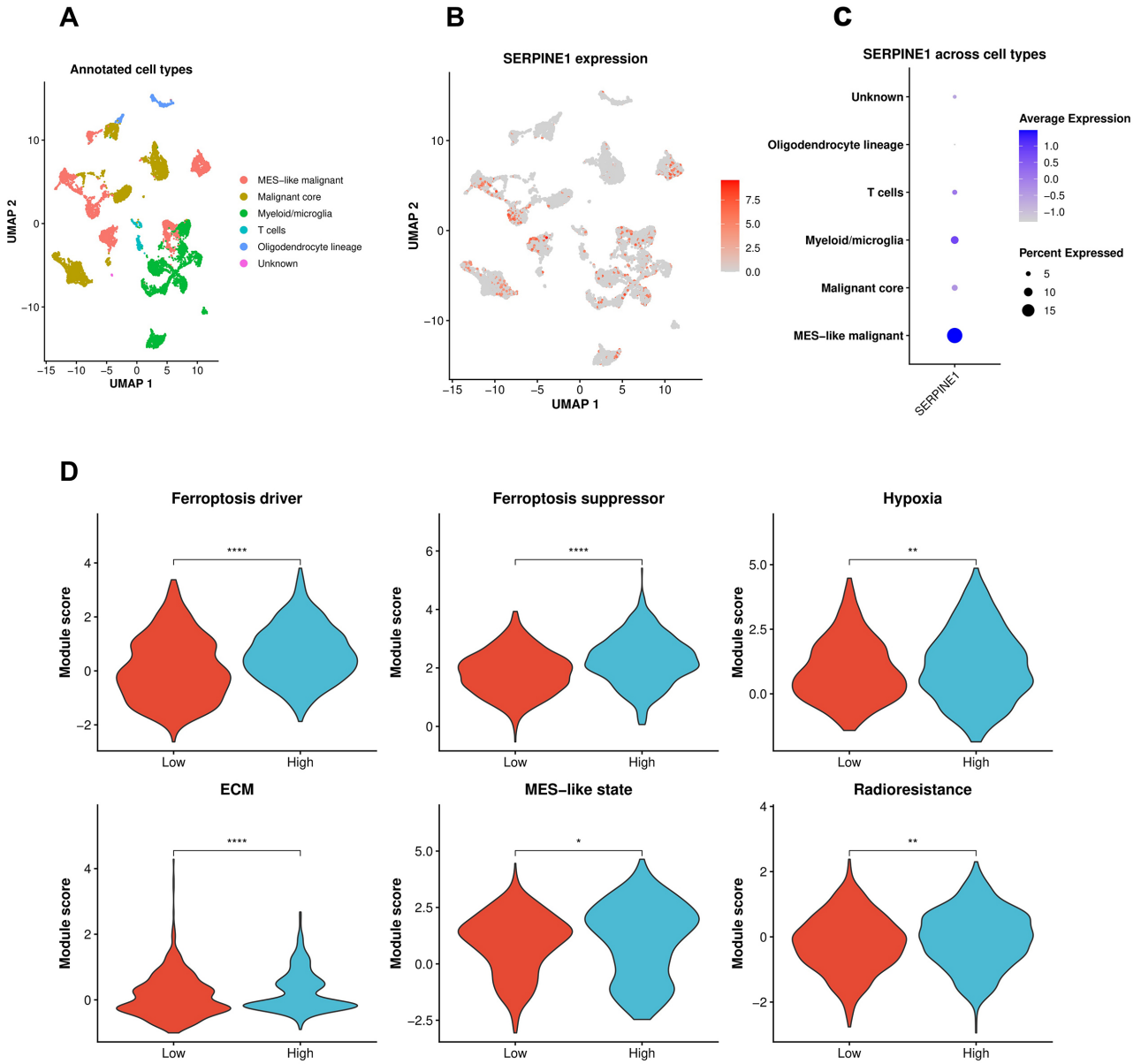

Fig. 8. Single-cell analysis of *SERPINE1* expression and associated functional states in glioblastoma. (A) UMAP visualization of annotated cell populations in a public IDH-wildtype GBM single-cell RNA-seq dataset. (B) Feature plot showing *SERPINE1* expression across GBM cell populations. (C) Dot plot showing *SERPINE1* expression across annotated cell types. *SERPINE1* was preferentially enriched in MES-like malignant cells, with weaker expression in myeloid/microglial cells. (D) Violin plots comparing functional module scores between *SERPINE1*-high and *SERPINE1*-low cells among *SERPINE1*-positive cells. *SERPINE1*-high cells showed significantly higher ferroptosis-driver, ferroptosis-suppressor, hypoxia, ECM, MES-like state, and radioresistance scores. Statistical significance was assessed using the Wilcoxon rank-sum test. *$p < 0.05$, **$p < 0.01$, ****$p < 0.0001$.

type signature, whereas it was negatively associated with the GBM proneural signature (Fig. 9C). Together, these findings indicate that *SERPINE1*-high GBM represents a microenvironmentally remodeled tumor state characterized by stromal activation, myeloid enrichment, hypoxia, ECM remodeling, and mesenchymal transition.

3.9 SERPINE1-associated Mesenchymal and Ferroptosis-defensive Remodeling is Linked to Clinical Radioresistance

Finally, we examined whether the *SERPINE1*-associated mesenchymal and ferroptosis-defensive state was related to clinically defined radiotherapy response. Selected TME and malignant phenotype signatures were compared between radiosensitive (RS) and radioresistant (RR) GBM groups. Among the analyzed signatures,

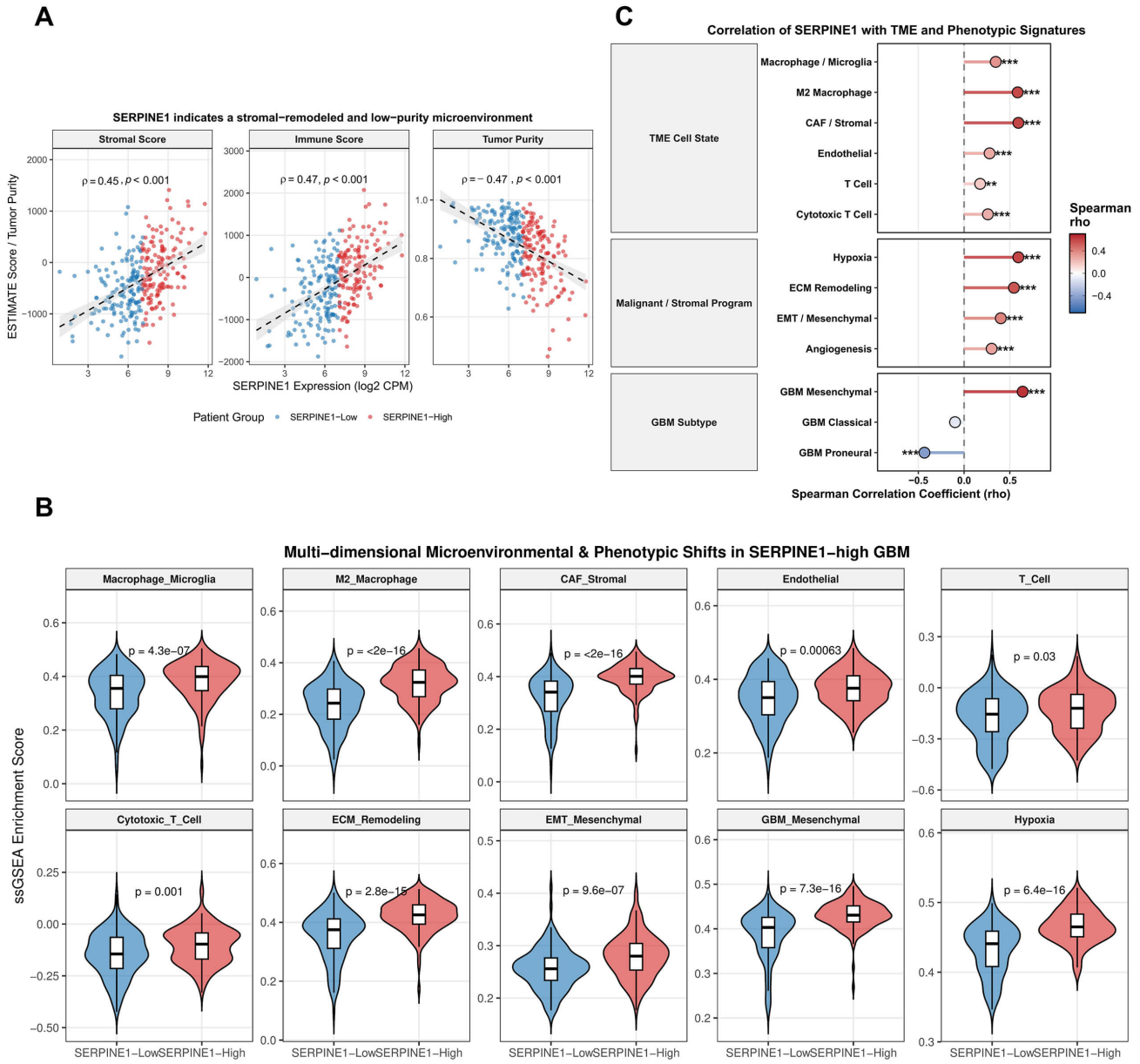

Fig. 9. *SERPINE1*-high GBM is associated with stromal remodeling, immune infiltration, hypoxia, and mesenchymal transition. (A) Correlations of *SERPINE1* expression with ESTIMATE-derived StromalScore, ImmuneScore, and tumor purity in the TCGA-GBM cohort. *SERPINE1* expression was positively correlated with StromalScore and ImmuneScore, but negatively correlated with tumor purity. (B) Violin plots comparing ssGSEA enrichment scores of tumor microenvironmental and malignant phenotype signatures between *SERPINE1*-low and *SERPINE1*-high GBM samples. *SERPINE1*-high tumors showed significantly higher macrophage/microglia, M2 macrophage, CAF/stromal, endothelial, T-cell, cytotoxic T-cell, ECM remodeling, EMT/mesenchymal, GBM mesenchymal, and hypoxia scores. Statistical significance was assessed using the Wilcoxon rank-sum test, and nominal *p*-values are shown. (C) Lollipop plot showing Spearman correlations between *SERPINE1* expression and tumor microenvironmental or phenotypic signature scores. Signatures were grouped into TME cell-state, malignant/stromal program, and GBM subtype categories. $^{**}p < 0.01$, $^{***}p < 0.001$.

only the GBM mesenchymal signature was significantly higher in RR tumors than in RS tumors (Fig. 10A; $p = 0.023$), whereas M2 macrophage, CAF/stromal, and hypoxia signatures did not differ significantly between the two groups. These results suggest that, within this cohort, radioresistance is more closely associated with mesenchymal transcriptional remodeling than with broad activation of the tested microenvironmental signatures.

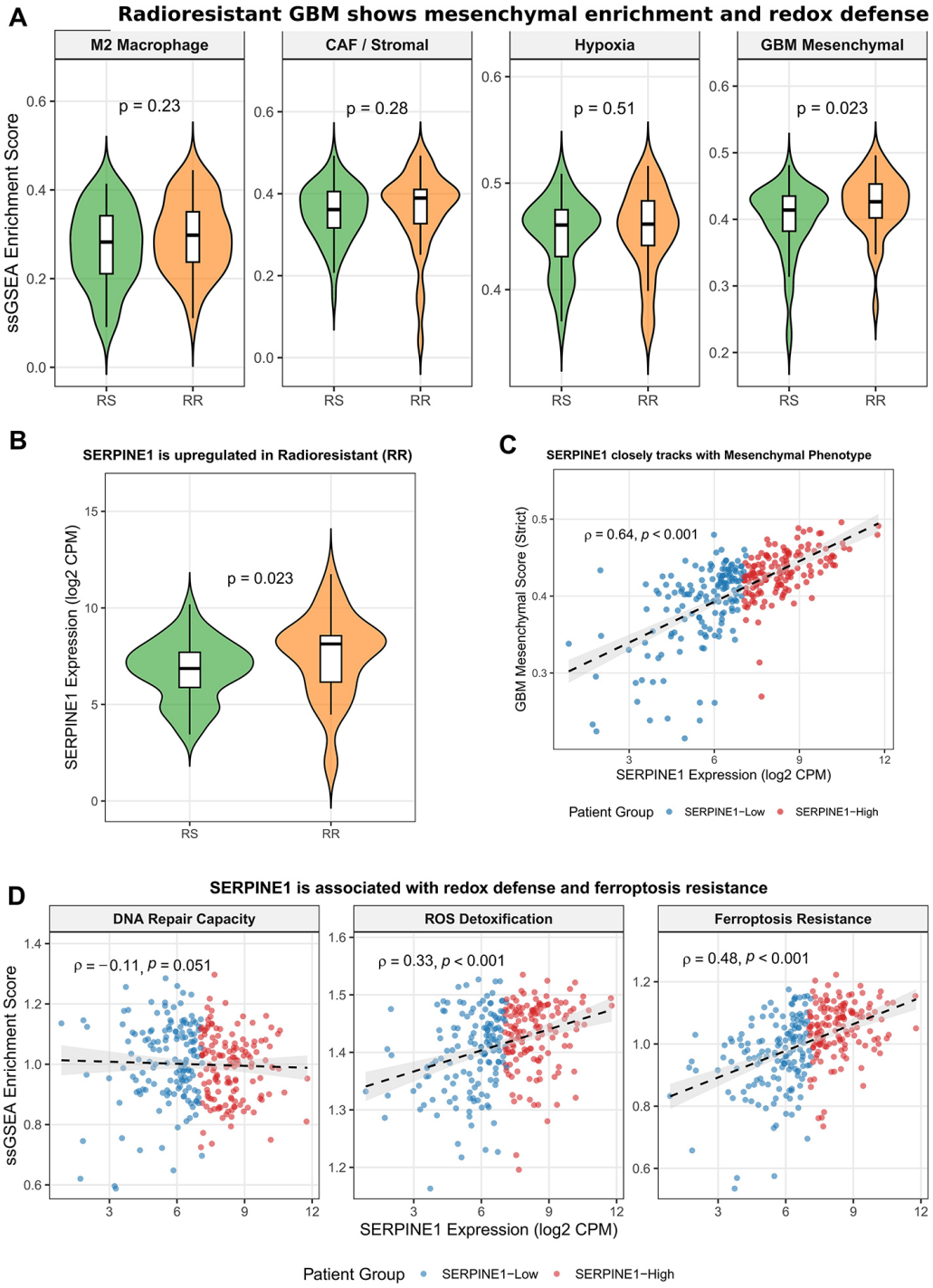

Fig. 10. SERPINE1 correlates with mesenchymal, redox-adaptive, ferroptosis-resistant, and radioresistant features in glioblastoma. (A) ssGSEA comparison between radiosensitive (RS) and radioresistant (RR) GBMs, revealing a significantly elevated mesenchymal score in the RR subset. (B) Significantly higher *SERPINE1* expression in RR compared to RS tumors. (C) Positive correlation of *SERPINE1* expression with the strict GBM mesenchymal score. (D) Mechanistic correlation analyses indicating that *SERPINE1* is positively linked to ROS detoxification and ferroptosis defense, independent of DNA repair capacity.

Consistent with this observation, *SERPINE1* expression was significantly higher in RR tumors than in RS tumors (Fig. 10B; $p = 0.023$). *SERPINE1* expression was also strongly correlated with the strict GBM mesenchymal signature score across GBM samples (Fig. 10C; $\rho = 0.64$, $p < 0.001$), supporting a close relationship between *SERPINE1* expression and mesenchymal transition. To further explore potential mechanisms linking *SERPINE1* to

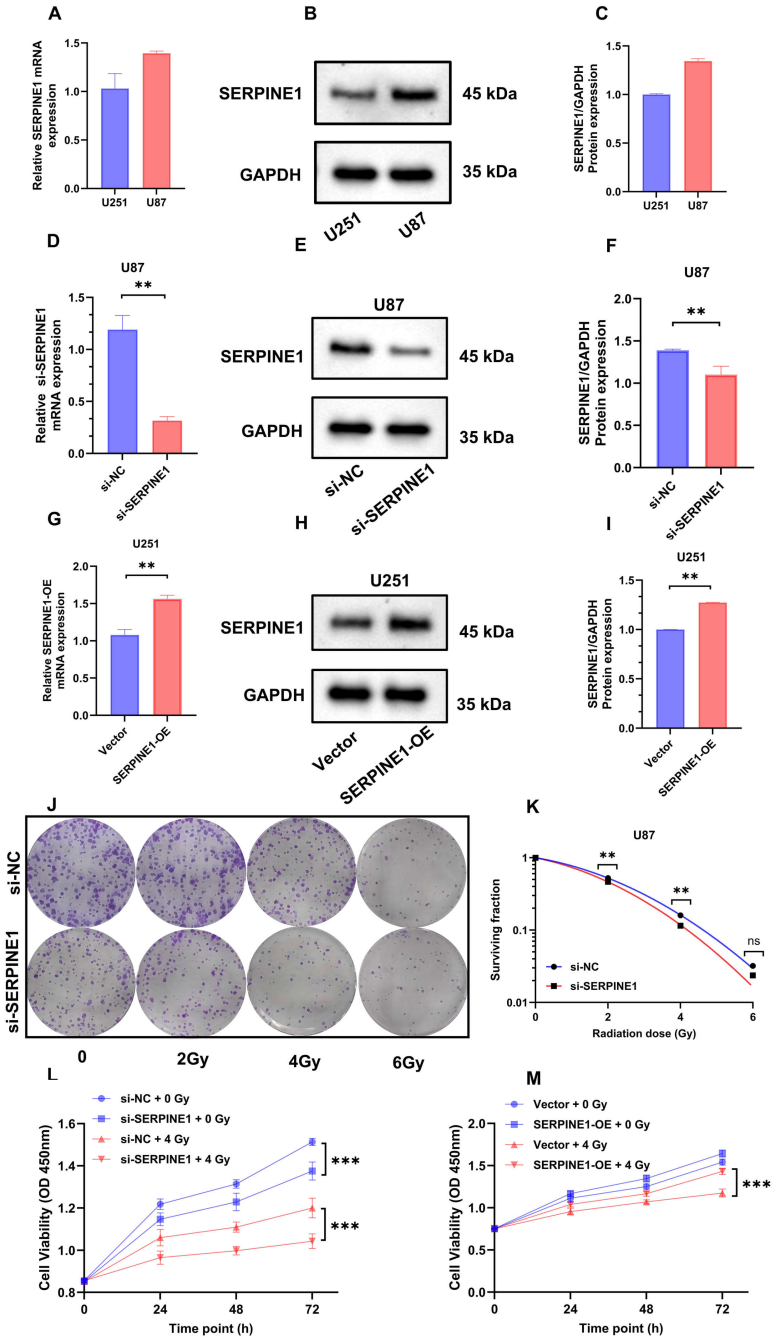

Fig. 11. *SERPINE1* dictates the radiation response in glioblastoma cells. (A) Basal *SERPINE1* mRNA expression in U251 and U87 cells. (B) Representative Western blot showing basal SERPINE1 protein levels. (C) Quantification of basal SERPINE1 protein expression normalized to GAPDH. (D) RT-qPCR validation of *SERPINE1* knockdown in U87 cells. (E) Western blot validation of SERPINE1 knockdown in U87 cells. (F) Quantification of SERPINE1 protein expression after knockdown. (G) RT-qPCR validation of *SERPINE1* overexpression in U251 cells. (H) Western blot validation of SERPINE1 overexpression in U251 cells. (I) Quantification of SERPINE1 protein expression after overexpression. (J) Representative clonogenic survival images for irradiated U87 cells. (K) Surviving fractions for U87 cells after 0, 2, 4, and 6 Gy X-ray irradiation fitted with the linear-quadratic model. (L) CCK-8 viability curves for U87 cells after *SERPINE1* knockdown and 4 Gy irradiation. (M) CCK-8 viability curves for U251 cells after *SERPINE1* overexpression and 4 Gy irradiation. Data are presented as mean ± SD from three independent biological replicates. Statistical significance was determined using Student's *t*-tests or one-/two-way ANOVA with Šídák's post-hoc correction, as appropriate. $^{**}p < 0.01$, $^{***}p < 0.001$; ns, not significant.

radioresistance, we analyzed mechanism-related signatures associated with DNA repair capacity, ROS detoxification, and ferroptosis resistance. *SERPINE1* expression was positively correlated with ROS detoxification and ferroptosis resistance signatures ($\rho = 0.33$ and $\rho = 0.48$, respectively; both $p < 0.001$), whereas DNA repair capacity was not positively associated with *SERPINE1* expression and showed only a weak negative trend ($\rho = –0.11$, $p = 0.051$) (Fig. 10D).

These findings suggest that *SERPINE1*-associated radioresistance in GBM is linked to mesenchymal remodeling and redox/ferroptosis-defense adaptation rather than enhanced DNA repair capacity. This transcriptional evidence provides a rationale for subsequent functional validation of whether *SERPINE1* modulates irradiation-induced ferroptosis and radiosensitivity in GBM cells.

3.10 SERPINE1 Knockdown Enhances Radiosensitivity Whereas SERPINE1 Overexpression Promotes Radioresistance in GBM Cells

We first assessed basal *SERPINE1* expression in U87 and U251 cells. RT-qPCR and Western blotting showed that SERPINE1 expression was higher in U87 cells than in U251 cells. Accordingly, U87 cells were used for *SERPINE1* knockdown, whereas U251 cells were used for *SERPINE1* overexpression in subsequent experiments. The efficiency of SERPINE1 silencing and overexpression was confirmed by RT-qPCR and Western blotting (Fig. 11A–I).

Clonogenic survival analysis in U87 cells showed that the surviving fraction decreased in a dose-dependent manner in both the si-NC and si-*SERPINE1* groups after irradiation. Compared with si-NC cells, *SERPINE1* knockdown significantly reduced the surviving fraction at 2 Gy ($52.37\% \pm 0.78\%$ vs. $46.50\% \pm 0.72\%$) and 4 Gy ($16.03\% \pm 0.25\%$ vs. $11.50\% \pm 0.36\%$), with both differences remaining significant after Šídák correction (adjusted $p < 0.001$). Although the surviving fraction of the si-*SERPINE1* group remained lower than that of the si-NC group at 6 Gy, the difference did not reach statistical significance (Fig. 11J,K).

Linear-quadratic model fitting further showed an overall downward shift of the survival curve in the si-*SERPINE1* group compared with the si-NC group. The fitted α and β values were 0.1922 and 0.06583 for the si-NC group and 0.2332 and 0.07527 for the si-*SERPINE1* group, respectively, with R^2 values of 0.9995 and 0.9996. These findings indicate that *SERPINE1* knockdown enhances the radiosensitivity of U87 cells.

Consistent with the clonogenic results, CCK-8 assays showed that 4 Gy irradiation reduced cell viability in U87 cells, and this inhibitory effect was further enhanced by *SERPINE1* knockdown (Fig. 11L). In contrast, *SERPINE1* overexpression in U251 cells attenuated the irradiation-induced reduction in cell viability (Fig. 11M).

3.11 SERPINE1 Knockown Enhances Irradiation-induced Ferroptosis-associated Lipid Peroxidation and Radiosensitivity in GBM Cells

In U87 cells, 4 Gy irradiation increased lipid ROS levels, MDA content, and intracellular Fe^{2+} accumulation. Compared with the si-NC + 4 Gy group, the si-*SERPINE1* + 4 Gy group showed further increases in all three parameters, indicating that *SERPINE1* knockdown enhanced irradiation-induced lipid peroxidation and iron accumulation. In contrast, although 4 Gy irradiation also increased lipid ROS, MDA, and Fe^{2+} levels in U251 cells, these changes were attenuated by *SERPINE1* overexpression (Fig. 12A–H).

Western blot analysis further showed that 4 Gy irradiation decreased the expression of HMOX1 and FTH1, while increasing ACSL4 expression. These changes were further enhanced by *SERPINE1* knockdown, as evidenced by additional downregulation of HMOX1 and FTH1 and further upregulation of ACSL4 in the si-*SERPINE1* + 4 Gy group compared with the si-NC + 4 Gy group (Fig. 12I,J).

To determine whether the radiosensitizing effect of *SERPINE1* knockdown involved ferroptosis-associated lipid peroxidation, rescue experiments were performed using the ferroptosis inhibitor ferrostatin-1 (Fer-1). Compared with the si-NC + 4 Gy group, the si-*SERPINE1* + 4 Gy group exhibited increased lipid ROS accumulation and reduced clonogenic survival. Fer-1 treatment decreased lipid ROS levels and partially restored colony formation in the si-*SERPINE1* + 4 Gy group, whereas it had little effect on basal lipid ROS levels or clonogenic growth (Fig. 13A–D).

To further examine whether *SERPINE1* overexpression-mediated radioresistance could be reversed by ferroptosis induction, cells were treated with the ferroptosis inducer RSL3. Colony formation assays showed that *SERPINE1*-OE + 4 Gy cells had greater clonogenic survival than Vector + 4 Gy cells, indicating that *SERPINE1* overexpression improved post-irradiation survival. However, RSL3 markedly reduced colony formation in the *SERPINE1*-OE + 4 Gy group. Consistently, lipid ROS analysis showed that *SERPINE1* overexpression suppressed irradiation-induced lipid ROS accumulation, whereas RSL3 restored lipid ROS levels in *SERPINE1*-OE cells exposed to 4 Gy irradiation (Fig. 13E–H).

4. Discussion

Taken together, our findings indicate that *SERPINE1* contributes to radioresistance in GBM by maintaining a stress-adaptive mesenchymal phenotype and limiting radiation-induced ferroptosis-associated lipid peroxidation. This does not imply that *SERPINE1* is the sole determinant of treatment failure or that ferroptotic cell death has been conclusively proven in all model systems. Rather, supported by cohort-level expression profiles, single-cell localization, bidirectional gene perturbation experiments, and pharmacological modulation, our data suggest that SER-

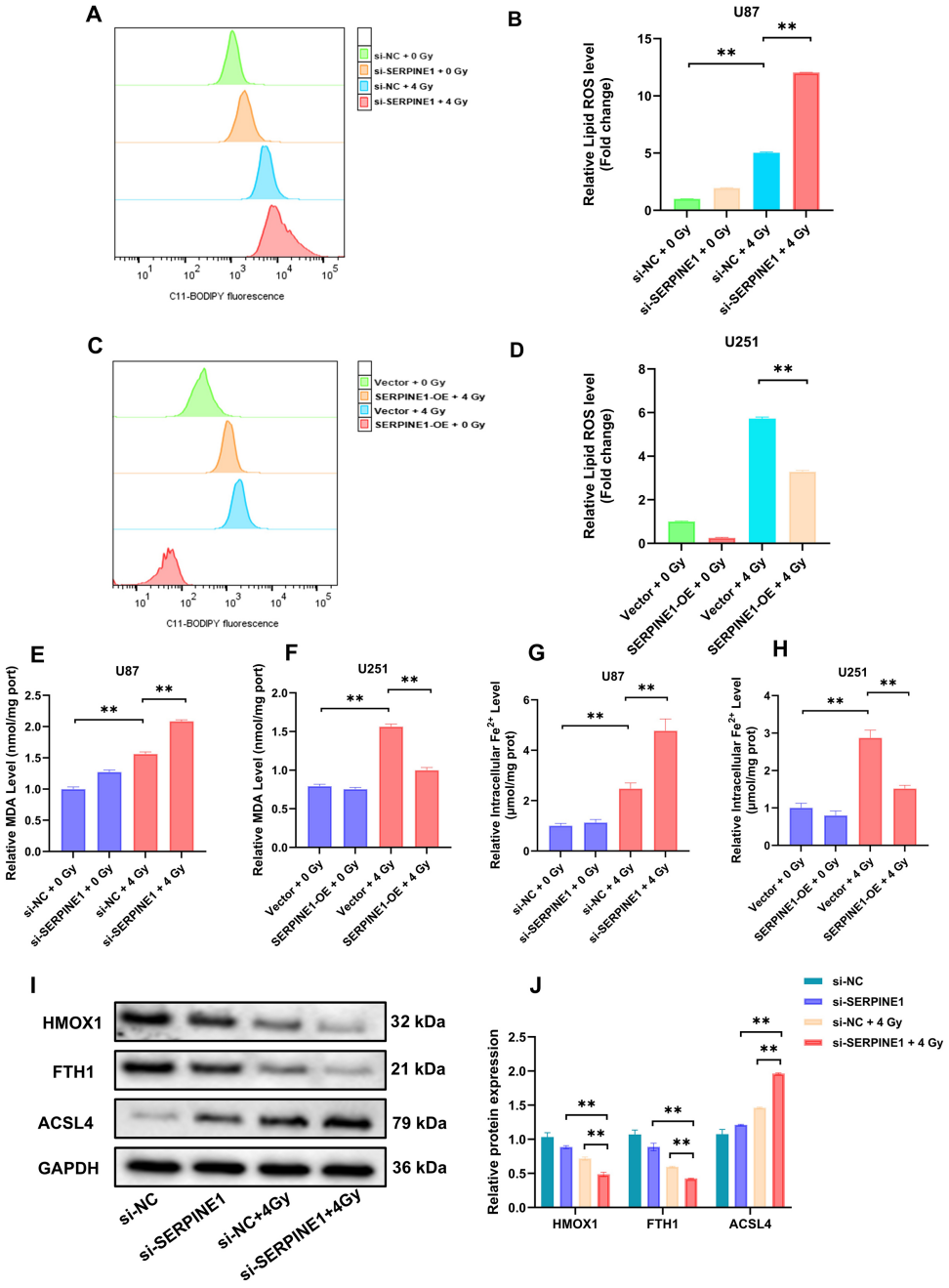

Fig. 12. ***SERPINE1*** **modulates irradiation-induced ferroptosis-associated lipid peroxidation and iron accumulation in GBM cells**. (A) Representative C11-BODIPY flow-cytometry histograms showing lipid ROS in U87 cells after *SERPINE1* knockdown and 4 Gy irradiation. (B) Quantification of relative lipid ROS levels in U87 cells. (C) Representative C11-BODIPY histograms showing lipid ROS in U251 cells after *SERPINE1* overexpression and 4 Gy irradiation. (D) Quantification of relative lipid ROS levels in U251 cells. (E,F) MDA levels in U87 and U251 cells, respectively. (G,H) Intracellular Fe^{2+} levels in U87 and U251 cells, respectively. (I) Western blot images showing HMOX1, FTH1, ACSL4, and GAPDH in U87 cells after *SERPINE1* knockdown and irradiation. (J) Quantification of ferroptosis-associated protein expression normalized to GAPDH. Data are presented as mean ± SD from three independent experiments. Statistical significance was determined using Student's *t*-test or ANOVA with appropriate post-hoc tests. $^{**}p < 0.01$.

PINE1 acts as a critical node within a broader adaptive resistance network. Ultimately, this study clarifies the association between SERPINE1 and aggressive GBM behavior and highlights a link between mesenchymal plasticity and ferroptosis-defense programs.

This study screened and identified *SERPINE1* by integrating differential expression analysis, weighted gene co-expression network analysis (WGCNA), and machine-learning feature ranking. We found that *SERPINE1* expression was significantly higher in glioblastoma (GBM) tissues

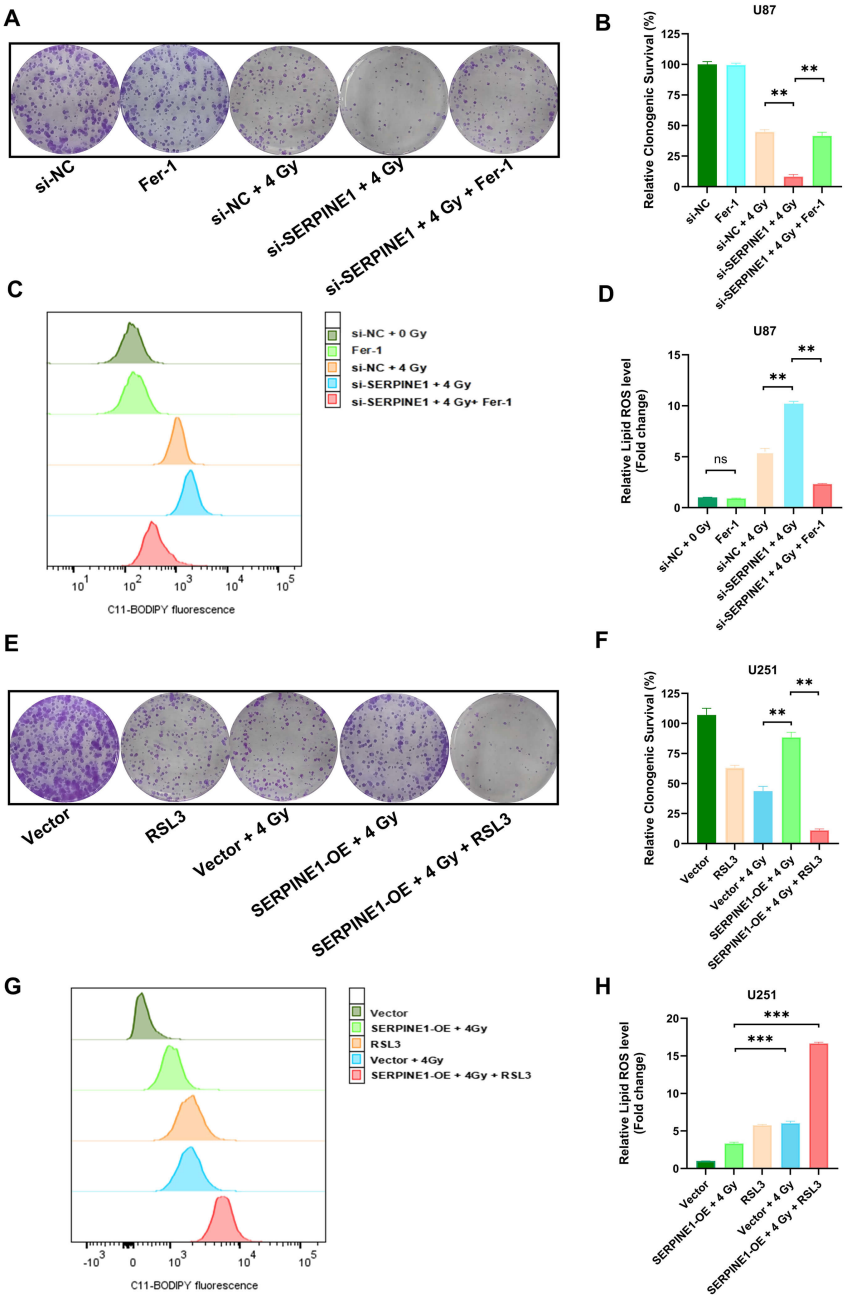

Fig. 13. Pharmacological modulation of ferroptosis-associated lipid peroxidation alters *SERPINE1*-dependent radiosensitivity. (A) Representative colony-formation images from *SERPINE1*-silenced U87 cells treated with 4 Gy irradiation with or without Fer-1. (B) Quantification of relative clonogenic survival in U87 cells. (C) Representative C11-BODIPY flow-cytometry histograms showing lipid ROS in U87 cells after *SERPINE1* knockdown, irradiation, and Fer-1 treatment. (D) Quantification of relative lipid ROS levels in U87 cells. (E) Representative colony-formation images from *SERPINE1*-overexpressing U251 cells treated with 4 Gy irradiation with or without RSL3. (F) Quantification of relative clonogenic survival in U251 cells. (G) Representative C11-BODIPY histograms showing lipid ROS in U251 cells after *SERPINE1* overexpression, irradiation, and RSL3 treatment. (H) Quantification of relative lipid ROS levels in U251 cells. Data are presented as mean ± SD from three independent experiments. Statistical significance was determined using Student's *t*-test, one-way ANOVA, or two-way ANOVA with Šídák's multiple-comparison test, as appropriate. $^{**}p < 0.01$, $^{***}p < 0.001$; ns, not significant.

than in normal brain tissues and was further upregulated in tumor samples clinically presenting as radiotherapy resistant. In multiple independent cohorts, high *SERPINE1* expression was significantly associated with shorter overall survival (OS). These observations are consistent with previous literature showing that *SERPINE1* is closely related

to the mesenchymal state of GBM and is an important factor driving tumor invasion and poor prognosis [20]. Furthermore, analysis of the *SERPINE1* network supports the involvement of *SERPINE1*-linked proteins in GBM pathogenesis and extracellular matrix-associated tumor progression [21]. Our findings extend these observations by linking *SERPINE1* to radiotherapy response and ferroptosis-associated redox adaptation.

A noteworthy finding of this study is that tumors with high *SERPINE1* expression showed simultaneous enrichment of ferroptosis drivers, markers, and suppressors. Although this molecular pattern may appear contradictory, it is biologically plausible. Ionizing radiation can induce strong lipid peroxidation and ferroptosis responses, and treatment-resistant tumors may exist in a ferroptosis-primed state [9,10,11,16,17,18,19]. We therefore hypothesize that *SERPINE1*-high GBM occupies a special adaptive equilibrium in which tumor cells experience continuous oxidative and iron-metabolism stress while activating compensatory ferroptosis-defense mechanisms. This coordinated enrichment of ferroptosis-related transcriptional features may reflect such a defensive state, and SERPINE1 knockdown may disrupt this equilibrium under irradiation.

Single-cell and tumor ecosystem analyses further clarified the cellular landscape of *SERPINE1* expression. *SERPINE1* was enriched in mesenchymal (MES)-like malignant cells, and *SERPINE1*-high cells showed activation of hypoxia, extracellular matrix remodeling, MES-like state, and radioresistance programs. Previous studies have considered MES-like states a core dimension of GBM cell plasticity, and longitudinal analyses have confirmed that therapeutic intervention can drive tumors toward a mesenchymal phenotype [7,39]. In the present study, only the core mesenchymal signature effectively distinguished radioresistant from radiosensitive tumors, whereas broader signatures such as M2 macrophages, cancer-associated fibroblast (CAF)/stromal programs, and hypoxia did not show the same stratification ability. This difference suggests that the *SERPINE1*-associated phenotype is linked to malignant-cell plasticity rather than simply to nonspecific stromal or immune infiltration. Nevertheless, *SERPINE1*-high tumors were positively correlated with stromal score, immune score, macrophage/microglia signatures, endothelial signatures, and hypoxic status, indicating that these tumors reside in a remodeled microenvironment that may further reinforce treatment resistance. Hypoxia signaling has also been shown to directly induce *SERPINE1* expression and promote GBM invasion [22,24].

SERPINE1 also appeared to participate selectively in redox adaptation independently of classical DNA repair programs. Because *SERPINE1* is a secreted serine protease inhibitor rather than a canonical ferroptosis regulator, its connection to ferroptosis is likely indirect. The present data support a model in which *SERPINE1*-high GBM cells are coupled to hypoxia, extracellular matrix remodeling, mesenchymal transition, ROS detoxification, and iron/lipid-peroxidation responses. Candidate downstream pathways that warrant direct testing include the NRF2-SLC7A11-GPX4 antioxidant axis, FSP1-CoQ10 defense, ACSL4-dependent lipid remodeling, and HMOX1/FTH1-associated iron handling. This result suggests that high *SERPINE1* expression contributes to GBM radioresistance primarily by maintaining redox homeostasis and limiting lipid peroxidation damage. This mechanism is consistent with the broader concept that hypoxia, metabolic reprogramming, and stress adaptation cooperate with classical DNA repair mechanisms to construct a multidimensional radioresistance network in GBM [4,5].

In vitro, *SERPINE1* knockdown significantly increased radiosensitivity, whereas *SERPINE1* overexpression produced a corresponding radioprotective effect. *SERPINE1* deficiency exacerbated radiation-induced lipid reactive oxygen species (ROS) accumulation, malondialdehyde (MDA) production, intracellular ferrous ion (Fe^{2+}) overload, and changes in ferroptosis-associated proteins. The ferroptosis inhibitor ferrostatin-1 partially rescued radiation-induced oxidative damage and loss of clonogenic ability, whereas the ferroptosis inducer RSL3 reversed the protective effect of *SERPINE1* overexpression. These results indicate that ferroptosis-associated lipid damage is a key component of *SERPINE1*-mediated radioresistance. This conclusion is consistent with prior studies showing that ferroptosis stress can sensitize hypoxic glioma cells to radiotherapy and that ionizing radiation itself can induce ferroptosis [40,41,42]. Although direct evidence for *SERPINE1*-mediated regulation of GBM ferroptotic cell death remains limited, studies in other solid tumors have shown that *SERPINE1*-related pathways can drive treatment resistance by inhibiting ferroptosis [43]. In preclinical GBM models, engineered cell-membrane nanovesicles loaded with *SERPINE1* inhibitors were reported to overcome temozolomide resistance, supporting a broader role for *SERPINE1* in therapeutic resistance [44].

5. Limitations

This study has several limitations. First, the radiotherapy-response analysis was retrospective and based on a relatively small discovery cohort, and RR/RS status was inferred from clinical response annotations rather than from prospective radiosensitivity testing. Second, TCGA and CGGA are legacy public datasets assembled across different diagnostic and molecular classification eras. MGMT promoter methylation data were insufficient in the TCGA radiotherapy-treated subset for inclusion in a statistically reliable multivariable Cox model. Therefore, residual diagnostic heterogeneity and unmeasured MGMT-related confounding cannot be fully excluded. The CGGA cohorts were used only as external validation datasets to confirm the association between *SERPINE1* expression and overall survival.

Third, the ferroptosis evidence is based on lipid ROS, MDA, Fe^{2+}, ferroptosis-associated proteins, and pharmacological agents with Fer-1 and RSL3. These data support ferroptosis-associated lipid peroxidation and ferroptosis-defense remodeling, but they do not by themselves conclusively establish ferroptotic cell death. Future studies should include additional ferroptosis-specific endpoints, such as GPX4 activity, SLC7A11/NRF2/FSP1 signaling, liproxstatin-1 rescue, and genetic rescue of ferroptosis regulators.

Fourth, the experimental validation was performed in U87 and U251 cells. These conventional long-term cell lines do not fully capture GBM heterogeneity, therapy-induced cell-state plasticity, or the tumor microenvironment. Validation in patient-derived GBM stem-like cells, organoids, primary cultures, and patient-derived xenografts will be required to define *SERPINE1*-dependent redox homeostasis and iron-metabolism pathways after radiotherapy. Biomarker-guided translational studies are also needed to evaluate the clinical potential of targeting *SERPINE1* or inducing ferroptosis as a radiosensitization strategy.

6. Conclusions

This study identified *SERPINE1* as a key mediator of radiotherapy resistance and ferroptosis-associated redox defense in GBM. By integrating radiotherapy-response transcriptomics, co-expression analysis, machine-learning prioritization, ferroptosis annotation, survival validation, scRNA-seq, tumor microenvironment characterization, and functional experiments, we found that *SERPINE1* is associated with poor prognosis, a MES-like GBM phenotype, hypoxia adaptation, redox homeostasis, and ferroptosis-defense programs. These findings support further investigation of *SERPINE1*-guided ferroptosis-based radiosensitization strategies in GBM.

Abbreviations

GBM, glioblastoma; TCGA, The Cancer Genome Atlas; CGGA, Chinese Glioma Genome Atlas; RR, radiotherapy-resistant; RS, radiotherapy-sensitive; DEG, differentially expressed gene; WGCNA, weighted gene co-expression network analysis; RRRG, radiotherapy resistance-related gene; GSEA, gene set enrichment analysis; OS, overall survival; ROC, receiver operating characteristic; Fer-1, ferrostatin-1; MDA, malondialdehyde; ROS, reactive oxygen species; ACSL4, acyl-CoA synthetase long-chain family member 4; FTH1, ferritin heavy chain 1; HMOX1, heme oxygenase 1; PAI-1, plasminogen activator inhibitor-1; scRNA-seq, single-cell RNA sequencing; TME, tumor microenvironment; ssGSEA, single-sample gene set enrichment analysis; MES, mesenchymal; ECM, extracellular matrix.

Availability of Data and Materials

All bioinformatic and clinical datasets supporting the conclusions of this article are available in public repositories. The scRNA-seq matrix is hosted in GEO (ID: GSE131928; https://www.ncbi.nlm.nih.gov/geo/query/acc.cgi?acc=GSE131928). Glioblastoma bulk RNA-seq and patient survival records were downloaded from the GDC Data Portal for the TCGA-GBM cohort (https://portal.gdc.cancer.gov/) and the CGGA platform (http://www.cgga.org.cn/). Additional primary data generated during the functional validation phase will be made available by the corresponding authors without undue reservation.

Author Contributions

YW and YL contributed to the conceptualization, methodology, software, validation, formal analysis, investigation, resources, data curation, writing—original draft preparation, writing—review and editing, and visualization; MD, CZ and ZJ contributed to the data curation, QZ and WY contributed to the conceptualization, supervision and project administration. All authors contributed to editorial changes in the manuscript. All authors read and approved the final manuscript. All authors have participated sufficiently in the work and agreed to be accountable for all aspects of the work.

Ethics Approval and Consent to Participate

Ethical review and approval were waived for this study because the human transcriptomic and clinical data used in the study were publicly available from the TCGA, CGGA, CPTAC, and GEO databases, and written informed consent had been obtained by the original investigators of those constituent datasets. The in vitro experiments used established, authenticated U87 and U251 human glioblastoma cell lines supplied by the Institute of Modern Physics, Chinese Academy of Sciences; no human participants, identifiable human materials, or newly collected clinical specimens were involved. Therefore, no additional human-subject ethics approval was required.

Acknowledgment

The authors thank all contributors to the TCGA, CGGA, CPTAC, and GEO datasets for providing data for this bioinformatics analysis.

Funding

This research received no external funding.

Conflicts of Interest

The authors declare no conflicts of interest.

Declaration of AI and AI-Assisted Technologies in the Writing Process

During the preparation of this work, the authors used ChatGPT to assist with formatting the manuscript according to the FBL article template and to check spelling and grammar. After using this tool, the authors reviewed and edited the content as needed and take full responsibility for the content of the publication.

Supplementary Material

Supplementary material associated with this article can be found, in the online version, at https://doi.org/10.31083/FBL53668.

References

[1] Weller M, Wen PY, Chang SM, Dirven L, Lim M, Monje M, et al. Glioma. Nature Reviews. Disease Primers. 2024; 10: 33. https://doi.org/10.1038/s41572-024-00516-y

[2] Schaff LR, Mellinghoff IK. Glioblastoma and Other Primary Brain Malignancies in Adults: A Review. JAMA. 2023; 329: 574–587. https://doi.org/10.1001/jama.2023.0023

[3] Stupp R, Mason WP, van den Bent MJ, Weller M, Fisher B, Taphoorn MJB, et al. Radiotherapy plus concomitant and adjuvant temozolomide for glioblastoma. The New England Journal of Medicine. 2005; 352: 987–996. https://doi.org/10.1056/NEJMoa043330

[4] Ali MY, Oliva CR, Noman ASM, Allen BG, Goswami PC, Zakharia Y, et al. Radioresistance in Glioblastoma and the Development of Radiosensitizers. Cancers. 2020; 12: 2511. https://doi.org/10.3390/cancers12092511

[5] Chédeville AL, Madureira PA. The Role of Hypoxia in Glioblastoma Radiotherapy Resistance. Cancers. 2021; 13: 542. https://doi.org/10.3390/cancers13030542

[6] Bhat KPL, Balasubramaniyan V, Vaillant B, Ezhilarasan R, Hummelink K, Hollingsworth F, et al. Mesenchymal differentiation mediated by NF-κB promotes radiation resistance in glioblastoma. Cancer Cell. 2013; 24: 331–346. https://doi.org/10.1016/j.ccr.2013.08.001

[7] Neftel C, Laffy J, Filbin MG, Hara T, Shore ME, Rahme GJ, et al. An Integrative Model of Cellular States, Plasticity, and Genetics for Glioblastoma. Cell. 2019; 178: 835–849.e21. https://doi.org/10.1016/j.cell.2019.06.024

[8] Dixon SJ, Lemberg KM, Lamprecht MR, Skouta R, Zaitsev EM, Gleason CE, et al. Ferroptosis: an iron-dependent form of nonapoptotic cell death. Cell. 2012; 149: 1060–1072. https://doi.org/10.1016/j.cell.2012.03.042

[9] Zhou Q, Meng Y, Li D, Yao L, Le J, Liu Y, et al. Ferroptosis in cancer: From molecular mechanisms to therapeutic strategies. Signal Transduction and Targeted Therapy. 2024; 9: 55. https://doi.org/10.1038/s41392-024-01769-5

[10] Ye LF, Chaudhary KR, Zandkarimi F, Harken AD, Kinslow CJ, Upadhyayula PS, et al. Radiation-Induced Lipid Peroxidation Triggers Ferroptosis and Synergizes with Ferroptosis Inducers. ACS Chemical Biology. 2020; 15: 469–484. https://doi.org/10.1021/acschembio.9b00939

[11] Lei G, Mao C, Yan Y, Zhuang L, Gan B. Ferroptosis, radiotherapy, and combination therapeutic strategies. Protein & Cell. 2021; 12: 836–857. https://doi.org/10.1007/s13238-021-00841-y

[12] Lv D, Zhong C, Dixit D, Yang K, Wu Q, Godugu B, et al. EGFR promotes ALKBH5 nuclear retention to attenuate N6-methyladenosine and protect against ferroptosis in glioblastoma. Molecular Cell. 2023; 83: 4334–4351.e7. https://doi.org/10.1016/j.molcel.2023.10.025

[13] Sun S, Gao T, Pang B, Su X, Guo C, Zhang R, et al. RNA binding protein NKAP protects glioblastoma cells from ferroptosis by promoting SLC7A11 mRNA splicing in an m^6A-dependent manner. Cell Death & Disease. 2022; 13: 73. https://doi.org/10.1038/s41419-022-04524-2

[14] Zhang Y, Kong Y, Ma Y, Ni S, Wikerholmen T, Xi K, et al. Loss of COPZ1 induces NCOA4 mediated autophagy and ferroptosis in glioblastoma cell lines. Oncogene. 2021; 40: 1425–1439. https://doi.org/10.1038/s41388-020-01622-3

[15] Li X, Zhang W, Xing Z, Hu S, Zhang G, Wang T, et al. Targeting SIRT3 sensitizes glioblastoma to ferroptosis by promoting mitophagy and inhibiting SLC7A11. Cell Death & Disease. 2024; 15: 168. https://doi.org/10.1038/s41419-024-06558-0

[16] Zhou Y, Zeng L, Cai L, Zheng W, Liu X, Xiao Y, et al. Cellular senescence-associated gene IFI16 promotes HMOX1-dependent evasion of ferroptosis and radioresistance in glioblastoma. Nature Communications. 2025; 16: 1212. https://doi.org/10.1038/s41467-025-56456-y

[17] Feng W, Liu Y, Zhang Q, Hu S, Xie D, Tan P, et al. GDF15 Drives Glioblastoma Radioresistance by Inhibiting Ferroptosis and Remodeling the Immune Microenvironment. International Journal of Biological Sciences. 2025; 21: 6794–6807. https://doi.org/10.7150/ijbs.115721

[18] Dong Q, Huo J, Yan Z, Li J, Chen X, Li L, et al. POT1-AS1/IGF2BP2/GPX4 promotes temozolomide resistance and radioresistance in glioblastoma by inhibiting ferroptosis. International Journal of Radiation Biology. 2026; 102: 49–60. https://doi.org/10.1080/09553002.2025.2588395

[19] D'Aprile S, Denaro S, Lavoro A, Candido S, Giallongo S, Torrisi F, et al. Glioblastoma mesenchymal subtype enhances antioxidant defence to reduce susceptibility to ferroptosis. Scientific Reports. 2024; 14: 20770. https://doi.org/10.1038/s41598-024-72024-8

[20] Seker F, Cingoz A, Sur-Erdem İ, Erguder N, Erkent A, Uyulur F, et al. Identification of *SERPINE1* as a Regulator of Glioblastoma Cell Dispersal with Transcriptome Profiling. Cancers. 2019; 11: 1651. https://doi.org/10.3390/cancers11111651

[21] Khosravi Z, Kaliaperumal C, Kumar AH. Analysing the role of SERPINE1 network in the pathogenesis of human glioblastoma. bioRxiv. 2022. https://doi.org/10.1101/2022.12.19.520990 (preprint)

[22] Zhang L, Cao Y, Guo X, Wang X, Han X, Kanwore K, et al. Hypoxia-induced ROS aggravate tumor progression through HIF-1α-SERPINE1 signaling in glioblastoma. Journal of Zhejiang University. Science. B. 2023; 24: 32–49. https://doi.org/10.1631/jzus.B2200269

[23] Guo X, Zhou H, Liu Y, Xu W, Kanwore K, Zhang L. Glial-Cell-Line-Derived Neurotrophic Factor Promotes Glioblastoma Cell Migration and Invasion via the SMAD2/3-SERPINE1-Signaling Axis. International Journal of Molecular Sciences. 2024; 25: 10229. https://doi.org/10.3390/ijms251810229

[24] Tao Z, Sun Y, Yilamu Y, Xu B, Yu C, Zhang H, et al. SERPINE1 maintained expression by NR4A1 promotes invasion and migration of glioblastoma in hypoxic microenvironment. Frontiers in Oncology. 2026; 15: 1750546. https://doi.org/10.3389/fonc.2025.1750546

[25] Cancer Genome Atlas Research Network. Comprehensive genomic characterization defines human glioblastoma genes and core pathways. Nature. 2008; 455: 1061–1068. https://doi.org/10.1038/nature07385

[26] Zhao Z, Zhang KN, Wang Q, Li G, Zeng F, Zhang Y, et al. Chinese Glioma Genome Atlas (CGGA): A Comprehensive Resource with Functional Genomic Data from Chinese Glioma Patients. Genomics, Proteomics & Bioinformatics. 2021; 19: 1–12. https://doi.org/10.1016/j.gpb.2020.10.005

[27] Robinson MD, McCarthy DJ, Smyth GK. edgeR: a Bioconductor package for differential expression analysis of digital gene expression data. Bioinformatics (Oxford, England). 2010; 26: 139–140. https://doi.org/10.1093/bioinformatics/btp616

[28] Law CW, Chen Y, Shi W, Smyth GK. voom: Precision weights unlock linear model analysis tools for RNA-seq read counts. Genome Biology. 2014; 15: R29. https://doi.org/10.1186/gb-2014-15-2-r29

[29] Ritchie ME, Phipson B, Wu D, Hu Y, Law CW, Shi W, et al. limma powers differential expression analyses for RNA-sequencing and microarray studies. Nucleic Acids Research. 2015; 43: e47. https://doi.org/10.1093/nar/gkv007

[30] Yu G, Wang LG, Han Y, He QY. clusterProfiler: an R package for comparing biological themes among gene clusters. Omics : a Journal of Integrative Biology. 2012; 16: 284–287. https://doi.org/10.1089/omi.2011.0118

[31] Langfelder P, Horvath S. WGCNA: an R package for weighted correlation network analysis. BMC Bioinformatics. 2008; 9: 559. https://doi.org/10.1186/1471-2105-9-559

[32] Tibshirani R. Regression Shrinkage and Selection Via the Lasso. Journal of the Royal Statistical Society Series B: Statistical Methodology. 1996; 58: 267–288. https://doi.org/10.1111/j.2517-6161.1996.tb02080.x

[33] Breiman L. Random forests. Machine Learning. 2001; 45: 5–32. https://doi.org/10.1023/A:1010933404324

[34] Cortes C, Vapnik V. Support-vector networks. Machine Learning. 1995; 20: 273–297. https://doi.org/10.1007/BF00994018

[35] Zhou N, Bao J. FerrDb: a manually curated resource for regulators and markers of ferroptosis and ferroptosis-disease associations. Database : the Journal of Biological Databases and Curation. 2020; 2020: baaa021. https://doi.org/10.1093/database/baaa021

[36] Cox DR. Regression models and life-tables. Journal of the Royal Statistical Society: Series B (Methodological). 1972; 34: 187–202. https://doi.org/10.1111/j.2517-6161.1972.tb00899.x

[37] Heagerty PJ, Lumley T, Pepe MS. Time-dependent ROC curves for censored survival data and a diagnostic marker. Biometrics. 2000; 56: 337–344. https://doi.org/10.1111/j.0006-341x.2000.00337.x

[38] Subramanian A, Tamayo P, Mootha VK, Mukherjee S, Ebert BL, Gillette MA, et al. Gene set enrichment analysis: a knowledge-based approach for interpreting genome-wide expression profiles. Proceedings of the National Academy of Sciences of the United States of America. 2005; 102: 15545–15550. https://doi.org/10.1073/pnas.0506580102

[39] Wang L, Jung J, Babikir H, Shamardani K, Jain S, Feng X, et al. A single-cell atlas of glioblastoma evolution under therapy reveals cell-intrinsic and cell-extrinsic therapeutic targets. Nature Cancer. 2022; 3: 1534–1552. https://doi.org/10.1038/s43018-022-00475-x

[40] Huang W, He Y, Yang S, Xue X, Qin H, Sun T, et al. CA9 knockdown enhanced ionizing radiation-induced ferroptosis and radiosensitivity of hypoxic glioma cells. International Journal of Radiation Biology. 2023; 99: 1908–1924. https://doi.org/10.1080/09553002.2023.2235433

[41] Wang X, Shi W, Li M, Xin Y, Jiang X. RSL3 sensitizes glioma cells to ionizing radiation by suppressing TGM2-dependent DNA damage repair and epithelial-mesenchymal transition. Redox Biology. 2024; 78: 103438. https://doi.org/10.1016/j.redox.2024.103438

[42] Chen L, Lin W, Le Z, Wan F, Zhang H, Geng S, et al. Carbon ion combined photon radiotherapy induces ferroptosis via NCOA4-mediated ferritinophagy in glioblastoma. Redox Biology. 2025; 86: 103865. https://doi.org/10.1016/j.redox.2025.103865

[43] Zhu X, Wei J, Chen X, Zhang X, Li Z, Yang F, et al. ELK3-SERPINE1-PCBP2 axis promotes gefitinib resistance in lung cancer by inhibiting ferroptosis. International Immunopharmacology. 2026; 169: 115963. https://doi.org/10.1016/j.intimp.2025.115963

[44] Wen J, Wu D, Le Y, Yin Z, Chen M, Shen Y, et al. Engineered nanovesicles targeting SERPINE1 overcome temozolomide resistance in glioblastoma. Cellular Signalling. 2025; 132: 111763. https://doi.org/10.1016/j.cellsig.2025.111763